HHS Public Access

Author manuscript

Cell Rep. Author manuscript; available in PMC 2023 October 02.

Published in final edited form as:

Cell Rep. 2023 June 27; 42(6): 112596. doi:10.1016/j.celrep.2023.112596.

Mettl14-mediated m^{6}A modification ensures the cell-cycle progression of late-born retinal progenitor cells

Liang Li[1], **Yue Sun**[1,2], **Alexander E. Davis**[1], **Sahil H. Shah**[1], **Lobna K. Hamed**[1], **Man-Ru Wu**[1], **Cheng-Hui Lin**[1], **Jun B. Ding**[2], **Sui Wang**[1,3,*]

[1]Department of Ophthalmology, Mary M. and Sash A. Spencer Center for Vision Research, Byers Eye Institute, Stanford University, Stanford, CA 94304, USA

[2]Department of Neurosurgery, Department of Neurology and Neurological Sciences, Stanford University, Stanford, CA 94305, USA

[3]Lead contact

SUMMARY

Neural progenitor cells lengthen their cell cycle to prime themselves for differentiation as development proceeds. It is currently not clear how they counter this lengthening and avoid being halted in the cell cycle. We show that N^6-methyladenosine (m^{6}A) methylation of cell-cycle-related mRNAs ensures the proper cell-cycle progression of late-born retinal progenitor cells (RPCs), which are born toward the end of retinogenesis and have long cell-cycle length. Conditional deletion of *Mettl14*, which is required for depositing m^{6}A, led to delayed cell-cycle exit of late-born RPCs but has no effect on retinal development prior to birth. m^{6}A sequencing and single-cell transcriptomics revealed that mRNAs involved in elongating the cell cycle were highly enriched for m^{6}A, which could target them for degradation and guarantee proper cell-cycle progression. In addition, we identified *Zfp292* as a target of m^{6}A and potent inhibitor of RPC cell-cycle progression.

Graphical Abstract

*Correspondence: suiwang@stanford.edu.

AUTHOR CONTRIBUTIONS

S.W. and L.L. conceived and supervised the study. L.L., A.E.D., L.K.H., M.-R.W., C.-H.L., and S.W. designed and performed the experiments. Y.S. and S.W. performed the bioinformatics analyses. S.W., L.L., Y.S., S.H.S., and J.B.D. wrote the manuscript. All authors provided critical feedback.

DECLARATION OF INTERESTS

The authors declare no competing interests.

INCLUSION AND DIVERSITY

We support inclusive, diverse, and equitable conduct of research.

SUPPLEMENTAL INFORMATION

Supplemental information can be found online at https://doi.org/10.1016/j.celrep.2023.112596.

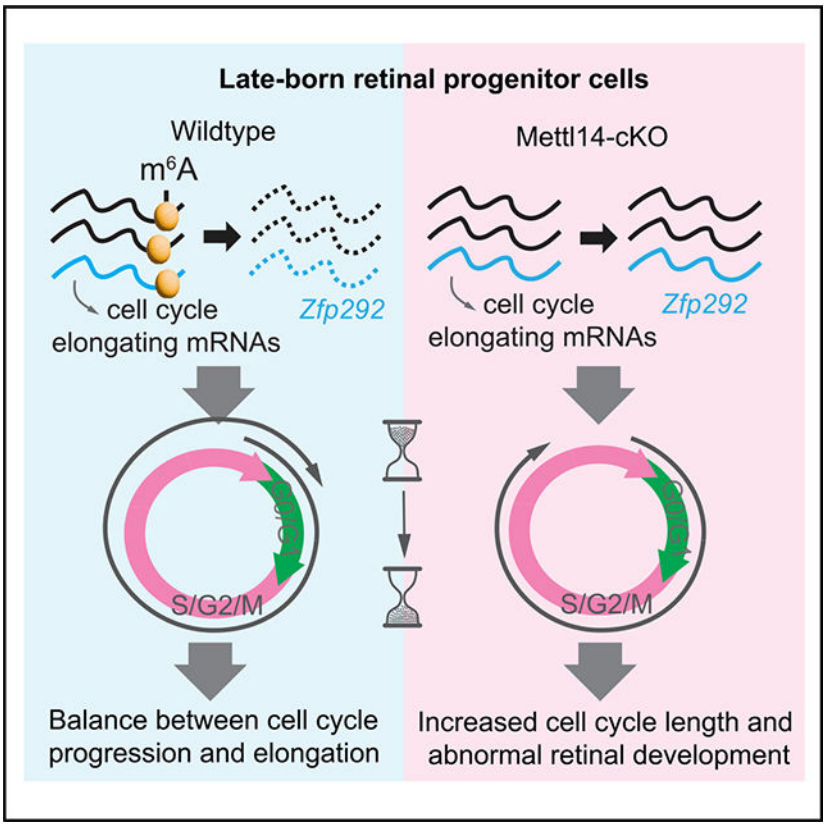

In brief

Retinal progenitor cells (RPCs) lengthen their cell cycle to prime themselves for differentiation as development proceeds. Li et al. report that Mettl14-mediated m^{6}A methylation regulates this process through modification of cell-cycle-related mRNAs. They identify *Zfp292* as a target of m^{6}A and an inhibitor of RPC cell-cycle progression.

INTRODUCTION

During central nervous system (CNS) development, the cell-cycle progression and differentiation of neural progenitor cells (NPCs) is precisely coordinated.[1–5] NPCs lengthen their cell cycle as development proceeds, which is necessary for accumulating differentiation-related factors and is seen across multiple cell lineages.[1,4] While many studies have focused on understanding cell-cycle lengthening and its association with differentiation, it is not clear how NPCs counter this lengthening and avoid excessive slowing of the cell cycle. An improved understanding of how NPCs offset cell-cycle lengthening and maintain continuous cell-cycle progression has broad implications for both fundamental cell biology and guiding future translational studies in cancer therapeutics and regeneration.

The neural retina is an ideal model to study the cell-cycle progression and differentiation of NPCs, as retinal progenitor cells (RPCs) can be easily manipulated by techniques such as *in vivo* electroporation and gamma-retrovirus-based lineage tracing.[6,7] The length of the

RPC cell cycle increases during retinal development from approximately 14 h at embryonic day 14 (E14) to about 30 h at early postnatal stages in rodent models.[8] This cell-cycle lengthening coincides with RPCs transitioning from early-born RPCs that differentiate into early-born neurons such as ganglion cells and cones, to late-born RPCs that differentiate into late-born cell fates including bipolar interneurons and Müller glial (MG) cells.[9] Although the exact mechanisms controlling the lengthening of the RPC cell cycle have yet to be elucidated, cell-cycle components, including cyclin, CDK, CDK inhibitors, transcription factors such as Vsx2, Pax6, Meis1/2, and Six3/6, epigenetic regulators, and differentiation-related genes all play important roles.[4] RPCs must counteract this cell-cycle lengthening to ensure proper cell-cycle progression, yet the mechanisms by which this process occurs are not well understood, especially in late-born RPCs that have an extended cell-cycle length.

One such candidate mechanism for regulating cell-cycle progression is post-transcriptional methylation of the sixth position of an adenine base, m^{6}A (N^6-methyladenosine), which is the most common internal modification on eukaryotic mRNAs and plays important roles in numerous biological processes including neural development.[10] It regulates many aspects of mRNA metabolism, including mRNA decay, translation, splicing, and nuclear export.[11] m^{6}A is deposited by the "writer" complex, which contains the core components Mettl3 (methyltransferase-like-3), Mettl14 (methyltransferase-like-14), and WTAP (Wilms' tumor 1-associating protein).[12] Deleting either *Mettl3* or *Mettl14* can deplete m^{6}A, and this depletion results in a prolonged cell cycle in neural stem cells in the cerebral cortex and extended neurogenesis in postnatal stages in *Mettl14*$^{f/f}$;*Nestin-Cre* mice.[13] Using the same transgenic mouse model, Wang et al. reported that depletion of m^{6}A in neural stem cells led to decreased proliferation and premature differentiation in the cortex.[14] While additional studies may be needed to further explore the exact consequences of manipulating m^{6}A, these studies strongly support the importance of m^{6}A in regulating the cell cycles of NPCs and encouraged us to examine the function of m^{6}A using RPCs as a model system.

Here we show that m^{6}A methylation on mRNAs is a key mechanism that enables late-born RPCs to counter cell-cycle lengthening. We conditionally deleted *Mettl14* in RPCs from the beginning of retinogenesis and found that m^{6}A modification ensures proper cell-cycle progression of late-born RPCs.

RESULTS

Depletion of Mettl14 induces retinal developmental delay and neuronal cell death

The genes involved in regulating m^{6}A dynamics are robustly expressed in the retina as revealed by quantitative PCR (qPCR) (Figures S1A and S1B). We detected the Mettl14 protein, a required component of the m^{6}A writer complex, in the retina starting from E12.5 through adulthood in most retinal cell types (Figures S1C and S1D). To study the function of m^{6}A in the retina, we generated a *Mettl14* conditional knockout mouse (Mettl14-cKO) by breeding *Mettl14*$^{f/f}$ mice with the *Chx10-Egfp/Cre* mouse line, which expresses EGFP and Cre recombinase simultaneously starting from approximately E13.5 in RPCs (Figure S1E).[15] We confirmed that the Mettl14 protein level was significantly reduced at E15.5 and postnatal day 0 (P0) in Mettl14-cKO retinas (*Mettl14*$^{f/f}$;*Chx10-Egfp/Cre*) compared with littermate controls (*Mettl14*$^{+/+}$;*Chx10-Egfp/Cre*) (Figure S1C). Total m^{6}A methylation levels were also

significantly lower in Mettl14-cKO retinas compared with controls (Figure S1F). Together, these experiments show that conditional knockout of *Mettl14* in RPCs can be used to study Mettl14-associated m^6A modification in the retina.

We examined the retinas of Mettl14-cKO mice at different developmental stages and in adults. Prior to birth, we did not observe any obvious defects in Mettl14-cKO retinas at E13.5 and E15.5 (Figures S1G and S1H). The number of $Otx2^+$ photoreceptor precursors and $Brn3a^+$ developing ganglion cells was not significantly different in Mettl14-cKO and control retinas (Figure S1I). At P0, the retinal thickness and the number of $Ki67^+$ RPCs were comparable between Mettl14-cKO and control retinas (Figures 1A and S1J). Therefore, Mettl14-mediated m^6A modification appears to be dispensable for prenatal retinal development.

As most RPCs exit the cell cycle and undergo differentiation by P7, we next asked how loss of *Mettl14* affected early postnatal retinal development. At this stage of development, the outer plexiform layer (OPL) is formed, and the outer nuclear layer (ONL) is separated from the inner nuclear layer (INL). In control retinas, we observed a nicely formed OPL at P7 as expected (Figure 1B). In Mettl14-cKO retinas, however, the OPL was not well formed (Figure 1B, yellow arrows). We also observed the appearance of rosette-like structures in the central retina, suggesting defects in early postnatal retinal development (Figure 1B, white arrows).

Finally, since retinal development continues until around P21 in mice, we asked how the retinas from Mettl14-cKO mice compared with the wild type soon after completion of retinal development and in later adulthood. At P21, Mettl14-cKO mice showed significantly decreased retinal thickness compared with those of controls (Figures 1C and 1E). The rosette-like structure observed at P7 spread to the peripheral regions of the retina and disappeared from the central regions (Figure 1C). In mature retinas (P56), the size of the Mettl14-cKO eyeball was reduced (Figure S1K) and the retina was even thinner compared with controls (Figures 1D and 1E). This was accompanied by the disappearance of the rosette-like structure. In approximately 30% of the Mettl14-cKO retinas, the ONL (where photoreceptors reside) only contained a few rows of cells (Figures 1D5 and S1L). Taken together, these histological analyses demonstrate that Mettl14 knockout affects both postnatal retinal development and the survival of mature retinal cells.

To further elucidate the postnatal developmental defects of Mettl14-cKO retinas, we immunostained the retinas at P7 with an antibody against Bassoon, a well-established marker for ribbon synapses residing in the OPL (Figure 2A).[16] The absence of Bassoon expression in P7 Mettl14-cKO further confirmed the delayed formation of the OPL (Figure 2B). In addition, most RPCs typically finish dividing by P7. Accordingly, Ki67 (a marker of cell proliferation) was rarely seen in the central and mid-peripheral regions of the control retinas at this stage (Figure 2C). However, we observed a significant number of $Ki67^+$ RPCs in these regions of Mettl14-cKO retinas at P7 (Figure 2C). These excessive P7 $Ki67^+$ cells also incorporated the thymidine analog 5-ethynyl-2′-deoxyuridine (EdU), which labels cells in the S phase of the cell cycle, further supporting their identities as RPCs (Figure 2C7).[17] These Mettl14-cKO RPCs eventually exited the cell cycle at around P10 (Figure

2D). Interestingly, despite significantly more Ki67$^+$ RPCs in Mettl14-cKO retinas at P7, the retinal thickness was unchanged at this time point and was in fact significantly reduced at P14 and P21 compared with controls (Figure 1E). Although the total number of retinal cells depends on cellular density in addition to retinal thickness, these findings encouraged us to examine cell death during postnatal retinal development. Before P10, we did not detect significantly increased overall cell death in Mettl14-cKO retinas compared with controls (Figure 2E). In fact, the apoptotic peaks at P5 and P9 in controls were delayed to P6 and P10, respectively, in Mettl14-cKO retinas (Figures 2E and S2A). After P10, the number of cells undergoing apoptosis was significantly higher in Mettl14-cKO retinas compared with controls at P14 and P21 (Figures 2E and S2A–S2C). Taken together, the delayed formation of OPL, excessive number of RPCs at P7, and normal but delayed occurrence of developmental apoptotic peaks all support the hypothesis that early postnatal retinal development is delayed in the absence of *Mettl14*.

We further examined whether late postnatal retinal cell differentiation and survival was affected by *Mettl14* depletion. The number of each major retinal cell type was quantified at P14, P21, and P56 (Figures 2F–2J, S2D, and S2E). The number of early-born neurons (born at prenatal stages), including retinal ganglion cells (RGCs) and horizontal cells (HCs), were comparable between Mettl14-cKO and control retinas at P14, but significantly decreased in Mettl14-cKO retinas starting from P21 (Figures 2F and 2G). The number of amacrine cells (born at both embryonic and early postnatal stages) and late-born bipolar cells (born at postnatal stages) at all three time points assayed were significantly decreased in Mettl14-cKO retinas (Figures 2H and 2I). Additionally, the number of photoreceptor cells was also significantly reduced in Mettl14-cKO compared with control as indicated by the reduced thickness of ONL at all three time points (Figure 1E). Notably, the number of Sox9$^+$ MG cells was consistently increased in Mettl14-cKO compared with control across all three stages (Figure 2J). Together, *Mettl14* conditional knockout promotes the formation of glial cells and significantly affects the survival of neurons in differentiated retinas.

Overall, we detected delayed retinal development and increased neuronal cell death in the differentiated retina when *Mettl14* was deleted (Figure 2K). Interestingly, *Mettl14* appeared to be only indispensable for postnatal retinal development. To further support this notion, we deleted the *Mettl14* gene in RPCs starting from P0 by *in vivo* electroporation. Electroporation primarily targets mitotic RPCs, as nuclear envelope breakdown is necessary for plasmids to enter nuclei.[6,18] We co-electroporated the *CAG-Cre and CAG-LoxP-stop-LoxP-GFP* (fluorescent reporter for Cre recombinase) plasmids into P0 *Mettl14*$^{f/f}$ or wild-type littermate mouse retinas *in vivo* (Figure S3A). At P7, we observed a significantly increased number of Ki67$^+$ cells in the electroporated portion of the *Mettl14*$^{f/f}$ retina but not in control retinas (Figure S3B). These experiments knocked out *Mettl14* from postnatal RPCs compared with Mettl14-cKO mice, which eliminated *Mettl14* expression starting at E13.5; however, we found similar RPC defects in both models at P7. Therefore, postnatal *Mettl14* knockout is sufficient for altering retinal development, further supporting the hypothesis that *Mettl14* is essential for postnatal retinal development.

Mettl14-depleted late-born RPCs have extended cell-cycle length

The presence of excessive RPCs in Mettl14-cKO retinas at P7 suggests that *Mettl14* plays key roles in regulating RPCs during postnatal retinal development. To investigate the underlying mechanisms, we traced the excessive RPCs found at P7 in Mettl14-cKO retinas using EdU pulse-chase assays. After EdU injection into Mettl14-cKO and control mice at P7, we harvested the retinas at P7 (2 h post EdU injection), P8 (24 h post EdU injection), P9 (48 h after EdU injection), and P10 (72 h after EdU injection) (Figure 3A). Retinal development progresses from the optic nerve head outward[19] with complete cell differentiation in the central and mid-peripheral regions of the retina by P7 in wild-type mice. As anticipated, we did not observe any EdU^+ nuclei in these regions in control mice on or after P7 (Figure 2C3, 2 h post EdU injection). In Mettl14-cKO retinas, a large number of EdU^+ nuclei were found in the central and mid-peripheral regions of the retina at P7 (Figure 2C7) indicating ongoing RPC proliferation. However, there was no increase of EdU^+ nuclei from P8 to P10, suggesting that EdU^+ P7 RPCs did not undergo division in Mettl14-cKO retinas (Figure 3B). The number of EdU^+ nuclei that were also $Ki67^+$ gradually decreased at P9 and P10, indicating that P7 Mettl14-cKO RPCs slowly exited the cell cycle (Figure 3C). These results suggest that P7 Mettl14-cKO RPCs have an extended cell-cycle length and eventually exit the cell cycle after a delay.

We next asked whether the increased cell-cycle length is a unique feature of P7 Mettl14-cKO RPCs or a general feature of postnatal late-born RPCs. We therefore traced RPCs at P3 in both control and Mettl14-cKO retinas using the same EdU pulse-chase assay as described above (Figure 3A). We injected EdU into Mettl14-cKO and control mice at P3 and harvested the retinas at P4 (24 h post EdU injection), P5 (48 h post EdU injection), and P6 (72 h after EdU injection) (Figures S3D and S3E). There were a significantly increased number of EdU/Ki67 double-positive cells in Mettl14-cKO retinas compared with controls at P5 and P6 (Figure S3F). This could be due to either increased proliferation or slower exit from the cell cycle. The total number of EdU^+ nuclei did not increase dramatically in Mettl14-cKO retinas compared with controls from P4 to P5 and P6 (Figure S3G), making proliferation an unlikely mechanism. Therefore, P3 Mettl14-cKO RPCs exited the cell cycle slower than control RPCs, similar to P7 Mettl14-cKO RPCs. We then directly examined the cell-cycle length of P3 Mettl14-cKO and control RPCs using the well-established fluorescent ubiquitination-based cell-cycle indicator (FUCCI).[20,21] We used the ubiquitous CAG promoter to drive the expression of FUCCI indicator (CAG-FUCCI), which labels G_1 phase nuclei with mCherry and $S/G_2/M$ phase nuclei with blue fluorescent protein (BFP) (Figure S4A). We electroporated the CAG-FUCCI plasmids into freshly dissected P3 retinas and cultured the retinas *ex vivo* (Figure S4B). By nature of the electroporation, RPCs receiving the CAG-FUCCI plasmids are primarily in M phase, creating a mostly synchronous population. The duration of G_1, S, G_2, and M phases of postnatal RPCs are approximately 8, 16, 3, and 2 h, respectively, in mice.[8] When we harvested the retinas at 24 h post electroporation, both control and Mettl14-cKO RPCs were BFP^+ (Figure S4C), suggesting that they were all in $S/G_2/M$ phase. At around 32 h post electroporation, FUCCI-labeled control RPCs turned on mCherry, indicating that they progressed to G_1 phase (Figure S4C). However, Mettl14-cKO RPCs were still primarily BFP^+ (Figure S4C), suggesting that their cell cycle progressed slower than in control RPCs. Combined with the

previous results from P7 retinas, these data further support that postnatal Mettl14-cKO RPCs have an extended cell-cycle length.

Finally, we investigated whether extended cell-cycle length would affect the fates of RPCs in Mettl14-cKO retinas. We labeled the excessive P7 RPCs in Mettl14-cKO retinas by EdU and traced their fates at P14, a time point when we can confidently assess cell fates by marker expression (Figures 3D and 3E). We found that P7 Mettl14-cKO RPCs located in the central and mid-peripheral regions of the retina had mainly differentiated into late-born bipolar cells (~23%) and MG cells (~38%) (Figure 3E). We also traced P1 control and Mettl14-cKO RPCs using replication-incompetent retroviruses (LIA-AP and LIA-Cre).[7,22] P1 Mettl14-cKO RPCs also favored late-born retinal fates (Figure S4D).

Overall, we show that postnatal late-born RPCs have an extended cell-cycle length and favor late-born retinal cell fates in the absence of *Mettl14*.

m^{6}A regulates cell-cycle-related genes in the developing retina

As *Mettl14* knockout depletes m^{6}A modifications, we profiled m^{6}A modified mRNAs at P7 in control and Mettl14-cKO retinas to investigate the underlying molecular mechanisms. Methylated RNA immunoprecipitation sequencing (MeRIP-seq or m^{6}A-seq), which uses an antibody against m^{6}A to immunoprecipitate m^{6}A-enriched mRNAs, allows for mapping of m^{6}A modified mRNAs in a genome-wide manner.[23] We combined this m^{6}A-seq with bulk RNA sequencing (RNA-seq) to identify the mRNAs that are modified by m^{6}A and differentially expressed in Mettl14-cKO retinas.

The m^{6}A modification was found to be enriched at the consensus RRACH motif (R = G or A; H = G, A, or C) in both control and Mettl14-cKO retinas at P7, which is consistent with studies in other systems (Figure 4A).[24,25] The overall landscape of m^{6}A was not changed in Mettl14-cKO, with m^{6}A modified sites primarily located at coding DNA sequences, stop codons, and 3′ untranslated regions (Figure 4B). In control P7 retinas, the mRNAs of approximately 79% of expressed genes contained significant levels of m^{6}A modification (Figure 4C). A total of 1,269 genes were differentially expressed in Mettl14-cKO retinas compared with controls. Among the 482 downregulated genes, approximately 12% of the genes showed significantly reduced m^{6}A levels. Gene ontology (GO) analyses showed that these downregulated genes were highly involved in circadian regulation of gene expression, blood vessel remodeling, and visual system development (Figure 4D). However, the reduction of m^{6}A levels showed no correlation with changes of mRNA levels in this group (data not shown). Among the 787 significantly upregulated genes, the mRNAs of 101 genes were m^{6}A modified and showed significantly reduced m^{6}A enrichment in Mettl14-cKO retinas. For these genes, the reduction of m^{6}A levels was correlated with increased mRNA levels, which is consistent with a major role of m^{6}A modification in mediating mRNA decay (Figure 4E). GO analyses revealed that these genes were highly involved in cell-cycle-related pathways, including cell division, regulation of cell-cycle process, and cellular response to DNA damage (Figure 4F). We confirmed the increased mRNA levels of top candidate genes in Mettl14-cKO retinas using qPCR (Figure 4G). Many are known to slow down the cell cycle, such as *Brca2, Brip1, Foxm1, Ttk*, and *Birc5* (Figure 4G).[26–30] The upregulation of these genes could explain the extended cell-cycle length of

Mettl14-cKO RPCs. Therefore, *Mettl14* deletion-mediated m^{6}A depletion resulted in high levels of mRNAs that typically function to slow down the cell cycle, suggesting a plausible mechanism by which Mettl14-cKO late-born RPCs maintain an extended cell-cycle length.

Single-cell RNA-seq reveals molecular events downstream of m^{6}A modification in the developing retina

As the m^{6}A-seq and bulk RNA-seq analyses did not offer cell-type specificity, we sought to identify the genes most relevant in RPCs. We performed single-cell transcriptomic analyses (scRNA-seq via 10x Genomics) to further dissect the *Mettl14* depletion-induced changes. We recovered 10,451 cells from four P7 control retinas and 13,116 cells from four Mettl14-cKO retinas. Based on well-established markers for developing retinal cell types,[31] we assigned known cell identities to the 25 clusters grouped by an unbiased clustering method (Seurat 4.1) (Figures S5A–S5D). The 11 RPC-derived cell types were selected for downstream analyses (Figures 5A–5C). In addition to the seven major retinal cell types (rod, cone, MG, bipolar, amacrine, horizontal, and ganglion cells), we detected cell clusters representing RPCs and precursors of rod, MG, and bipolar cells in P7 retinas. As Mettl14-cKO resulted in excessive RPCs at P7, we focused on analyzing the RPC and precursor cell clusters to elucidate the underlying mechanisms.

The scRNA-seq data supported our aforementioned histological and lineage-tracing findings (Figures 1, 2, and 3). First, there was an increased number of *Mki67*$^+$ (the gene encoding Ki67) RPCs in Mettl14-cKO retinas compared with controls (Figure 5D), which is consistent with the increased number of Ki67$^+$ RPCs in P7 Mettl14-cKO retinas. Second, the proportions of the precursor cells for rod, bipolar, and MG cells were all greater in Mettl14-cKO retinas compared with controls, suggesting a retinal development delay at P7 (Figure 5C). Third, the percentage of retinal cells with bipolar (bipolar plus bipolar precursors) or MG (MG plus MG precursors) cell fates was higher, whereas the percentage of cells with rod fate (rod plus rod precursors) was decreased in P7 Mettl14-cKO retinas compared with controls. This result further supports our previous finding that P7 Mettl14-cKO RPCs favor bipolar and MG cell fates. Lastly, the proportions of the cell types derived from early RPCs, such as ganglion cells and HCs were largely unaffected in P7 Mettl14-cKO retinas (Figure 5C), demonstrating that early RPCs were not affected by loss of *Mettl14*.

We next sought to identify RPC-specific targets of m^{6}A by analyzing the genes that were differentially expressed in the RPC cluster. From our previous m^{6}A-seq and bulk RNA-seq experiments, we had already defined a candidate list of cell-cycle-related genes from total retinas. We explored the expression of these genes within the defined RPC cluster and found an increase in expression in Mettl14-cKO RPCs compared with control RPCs (Figure S5E). scRNA-seq revealed additional genes that were significantly upregulated in Mettl14-cKO RPCs (Figure 5E). Most of these genes showed reduced m^{6}A levels based on m^{6}A-seq (Figure S5F). Some of these genes have been implicated in regulating the cell cycle in other systems,[32–36] but their roles in RPC cell-cycle progression have not been well studied.

In addition, we analyzed differentially expressed genes in each of the 11 cell-type clusters. Interestingly, *Cdkn1a*, which encodes the P21^{Cip1} protein and is well known for its role in inhibiting cell-cycle progression,[37] was upregulated in clusters classified as rod precursors

(rod-pre), bipolar precursors (BP-pre), MG precursors (MG-pre), and RPCs in Mettl14-cKO retinas compared with controls (Figures 5D and S5G). We confirmed the increased levels of *Cdkn1a* mRNA and protein in Mettl14-cKO retinas at P7 using qPCR and immunostaining (Figures 5F and S5H) and found that approximately 86% of Cdkna1$^+$ cells were Ki67$^+$ in Mettl14-cKO retinas at P7 (Figures S5I and S5J). It is thus likely that P21^{Cip1} upregulation also contributes to RPC cell-cycle extension in Mettl14-cKO retinas. Notably, m^{6}A-seq did not detect m^{6}A enrichment on *Cdkn1a* mRNAs (Figure 5G), suggesting that *Cdkn1a* is not directly regulated by m^{6}A in the retina.

Finally, we compared the P7 Mettl14-cKO RPCs with wild-type P0, P2, and P8 RPCs in published scRNA-seq datasets (Figure S6A).[31] The P7 Mettl14-cKO RPCs intermingled with wild-type RPCs as shown in the uniform manifold approximation and projection (UMAP) plot, suggesting that they are not dramatically different from wild-type RPCs at the global transcript level (Figures S6A–S6D). The cell-cycle scoring and regression analyses (Seurat 4.0.6) revealed that the percentage of P7 Mettl14 RPCs in the G_2/M phases of the cell cycle was higher than that in P7 control RPCs (Figure S6E). Notably, P7 Mettl14-cKO RPCs differentially expressed genes that are involved in the cellular senescence pathway compared with P0, P2, and P8 wild-type RPCs (Figure S6F). Given that P21^{Cip1} is a well-established senescence marker,[38] this result further suggests that P21^{Cip1}-related pathways may play important roles downstream of m^{6}A depletion in RPCs.

Taken together, the scRNA-seq analyses identified cell-cycle-related changes in Mettl14-cKO retinas and revealed additional targets of m^{6}A. These data also suggest that *Cdkn1a* could be an important contributor of m^{6}A-depletion-induced late-born RPC cell-cycle extension.

Zfp292 is a target of m^{6}A that inhibits RPC cell-cycle progression in the developing retina

scRNA-seq identified several potential targets of m^{6}A specifically in the RPC cluster (Figures 5D and 5E). One of these targets, *Zfp292*, was a particularly interesting candidate, as it is highly modified by m^{6}A in control retinas (Figure 5I) and its m^{6}A level reduced the most among the top ten upregulated genes in Mettl14-cKO RPCs (Figure S5E). *Zfp292* encodes the transcription factor zinc finger protein 292 (also known as Znf292). A few studies have identified *Zfp292* as a tumor-suppressor gene,[36,39,40] but its function in the retina or in the rest of CNS is unknown. We therefore sought to elucidate the function of *Zfp292* in RPCs during early postnatal retinal development.

We first examined the expression pattern and level of *Zfp292* in developing control and Mettl14-cKO retinas. *Zfp292* was expressed by most retinal cells, and its level was significantly upregulated in P7 Mettl14-cKO (Figure 5H). To better quantify Zfp292 mRNA levels in RPCs, we freshly dissociated control and Mettl14-cKO retinas into single cells, mounted the cells on glass slides, and performed quantitative mRNA *in situ* hybridization.[41,42] We probed for *Hes1*, a well-known marker for RPCs in the developing retina, as well as *Zfp292*. We quantified the number of fluorescent dots, which is positively correlated with mRNA levels, in each cell for both *Zfp292* and *Hes1* probes. The number of *Zfp292*$^+$ dots per cell was significantly increased in *Hes1*$^+$ RPCs but not in *Hes1*$^-$ retinal cells in Mettl14-cKO retinas (Figures 6A–6C). These data demonstrate that *Zfp292* mRNA

is upregulated in RPCs when m^6A is depleted by *Mettl14* knockout, consistent with the scRNA-seq results.

We next examined whether exogenous expression of *Zfp292* in wild-type retinas can phenocopy Mettl14-cKO retinas and increase the cell-cycle length of late-born RPCs. The plasmids overexpressing codon-optimized *Zfp292* (CAG-Zfp292-op) were constructed and delivered into P0 mouse retinas *ex vivo* via co-electroporation with CAG-GFP plasmids for identification (Figure 6D, referred to hereafter as "Zfp292-OE" condition). In this experimental paradigm, plasmids typically express in retinal cells 6–8 h after *ex vivo* electroporation. Twenty-four hours after the retinas were electroporated with either control or Zfp292-OE plasmids, we applied EdU to retinas for 1 h and harvested at 2, 30, or 60 h later to trace the cell cycle of late-born RPCs (Figure S7). As development proceeded, the number of GFP/EdU/Ki67 triple-positive cells decreased at a slower rate in Zfp292-OE retinas than in controls (Figure 6E), indicating that the RPCs overexpressing *Zfp292* exited the cell cycle slower. Importantly, the total number of GFP/EdU double-positive cells was not significantly higher in Zfp292-OE compared with control, suggesting that *Zfp292* did not promote RPC proliferation (Figures S7A–S7D). Based on these results, *Zfp292* overexpression can significantly inhibit late-born RPC cell-cycle progression, likely underlying the extended RPC cell-cycle length in Mettl14-cKO retinas.

To further explore how *Zfp292* inhibits RPC cell-cycle progression, we used RNA-seq to identify the downstream targets of Zfp292. Specifically, the control or Zfp292-OE plasmids (Figure 6D) were electroporated into P0 mouse pups *in vivo*. We harvested the retinas 4 days later to allow for robust expression, dissociated the retinas into single-cell preps, collected the GFP^+ RPCs via fluorescence-activated cell sorting from control or Zfp292-OE conditions, and processed the cells for bulk RNA-seq (Figures 6F and S7E–S7H). A total of 477 or 351 genes were significantly up- or downregulated, respectively, in Zfp292-OE compared with control RPCs (Figure 6G). GO analyses showed that the upregulated genes were highly involved in negative regulation of chromatid segregation and mitotic spindle checkpoint signaling (Figure 6H), while the downregulated genes were highly involved in retinal function and homeostasis (Figure 6I). These data suggest that Zfp292 may inhibit RPC cell-cycle progression by negatively regulating the M phase of the cell cycle.

Lastly, we examined the fates of RPCs overexpressing *Zfp292*. The control or Zfp292-OE plasmids (Figure 6D) were electroporated into P0 mouse pups *in vivo*. We harvested the retinas at P14 and quantified the number of GFP^+ cells that adopted rod, bipolar, amacrine, or MG cell fates. Zfp292-OE favored late-born MG cell fates (Figures S7I and S7J).

Taken together, *Zfp292* is highly upregulated in RPCs in *Mettl14* knockout. It inhibits RPC cell-cycle progression, likely by activating genes involved in negative regulation of M phase of the cell cycle.

DISCUSSION

We investigated the mechanisms by which NPCs counter cell-cycle lengthening during neural development. We showed that Mettl14-mediated m^6A modification is critical for

ensuring the proper cell-cycle progression of late-born RPCs. In wild-type late-born RPCs, the genes that function to increase cell-cycle length are upregulated via a variety of mechanisms to prime the cells for differentiation.[1,4] If this upregulation is uncontrolled, RPCs may not exit the cell cycle appropriately, disrupting normal retinal development. To counter this effect, RPCs use m^{6}A modification to downregulate the levels of cell-cycle-elongating mRNAs. As a result, the wild-type late-born RPCs can either exit or re-enter the cell cycle in a tightly coordinated manner (Figure 7).

When Mettl14-mediated m^{6}A was depleted in late-born RPCs, the balance between cell-cycle lengthening and cell-cycle progression was broken. The Mettl14-cKO RPCs therefore have extended cell-cycle length owing to the presence of high levels of genes that inhibit cell-cycle progression, such as *Zfp292*, as revealed in this study. Even though these mutant RPCs eventually exited the cell cycle and underwent differentiation, the effects of this extended cell-cycle length were remarkable. We observed significant developmental delay postnatally and increased production of late-born cell types. Overall, we establish m^{6}A as an important mechanism for ensuring the proper cell-cycle progression of late-born RPCs (Figure 7).

Early- and late-born RPCs are differently regulated by m^{6}A

m^{6}A appeared to be dispensable for RPCs that were born before birth (early-born RPCs). No significant defects were detected in the retina prior to or at birth even though Mettl14 was significantly reduced. It is possible that the m^{6}A-regulated genes that slow down the cell cycle are not highly expressed in early-born RPCs, as the cell-cycle length of early-born RPCs (~14 h) is much shorter than that of late-born RPCs (~30 h). Alternatively, the genes with the ability to increase cell-cycle length may not be regulated by m^{6}A in early-born RPCs. If either of these speculations is true, m^{6}A depletion would have no effect on early-born RPCs. To explore these possibilities, we examined the expression levels of m^{6}A-regulated genes (identified in late-born RPCs) in control and Mettl14-cKO retinas at E15.5 and P7 via qPCR (Figure S8A). Interestingly, some of the m^{6}A-regulated genes were expressed in low levels at E15.5 in control retinas compared with their levels at P7, while others were highly expressed. Nevertheless, none of the m^{6}A-regulated genes was differentially expressed in control and Mettl14-cKO retinas at E15.5. These results suggest that m^{6}A is not the dominant mechanism employed by the early-born RPCs to regulate cell-cycle-related genes. However, it would be interesting to explore time-dependent changes of m^{6}A modification throughout retinal development in future studies. Taken together, our work shows that early-born and late-born RPCs are differently regulated by m^{6}A. This further highlights the heterogeneity among RPCs as revealed by single-cell transcriptomic analyses.[31]

Context-dependent regulation by m^{6}A in the CNS

m^{6}A modification is a well-established mechanism in neural development. During cortical neurogenesis, depletion of m^{6}A via knockout of different components of the m^{6}A machinery resulted in two major outcomes. First, a prolonged cell cycle of embryonic NPCs and extended neurogenesis was found in *Mettl14* and *Fmr1* conditional knockout mice.[13,43] Second, deletion of *Mettl14* or *Ythdf2* resulted in reduced proliferation and

premature differentiation of NPCs.[44,45] During cerebellar development, m^{6}A modification downregulated apoptosis-related mRNAs and ensured the survival of newly generated cerebellar granule cells.[45] In our experiments, we observed extended cell-cycle length when Mettl14-mediated m^{6}A was depleted in RPCs, consistent with the findings from Yoon et al.[13] However, we only observed a partially extended neurogenesis in the retina, with a majority of the late-born Mettl14-cKO RPCs differentiating to bipolar interneurons and MG cells. We also observed significant neuronal cell death in Mettl14-cKO retinas starting from P14, similar to what has been reported during cerebellar development[45]; however, in the retina cell death continued to adulthood. It is possible that different cohorts of mRNAs are modified by m^{6}A in different tissues, or that the m^{6}A reader complex can process m^{6}A-modified mRNAs differently based on the context. Indeed, conditional deletion of an m^{6}A reader gene *Ythdf2* in RPCs led to increased RGC dendrite branching and a thicker inner plexiform layer during early postnatal development but did not affect the proliferation and differentiation of RPCs.[46]

Although manipulating writer and reader complexes both affect retinal development, additional studies are necessary to dissect why deleting different components of the m^{6}A pathway results in distinct phenotypical readouts. It would be important to reveal the mechanisms underlying this cell-type-specific regulation by m^{6}A in future studies. Overall, m^{6}A has overlapping functions in the retina and other regions of the CNS. As Mettl14-cKO mice can survive to adulthood, we have the opportunity to explore the importance of m^{6}A functionality in adult retina and in neurodegenerative diseases in the future.

Targets of m^{6}A for regulating RPC cell-cycle progression

Our study identified *Zfp292* as a target of m^{6}A in the developing retina. *Zfp292* can significantly inhibit the cell-cycle progression of late-born RPCs and can function via the activation of genes involved in negatively regulating the M phase of the cell cycle. It is possible that *Zfp292* is not solely responsible for the phenotype seen with loss of m^{6}A. By generating a short hairpin RNA knockdown construct against *Zfp292*, we asked whether decreasing the levels of *Zfp292* could rescue the developmental defects observed in Mettl14-cKO retinas. This led to a slightly (but not significantly) reduced number of Ki67$^+$ cells at P7 in Mettl14-cKO retinas, suggesting that additional m^{6}A-dependent genes must also contribute to the phenotypes observed in Mettl14-cKO retinas (Figures S8B–S8G). In addition, the RPCs with exogenous expression of *Zfp292* had extended cell-cycle length and favored MG cell fates at the expense of neuronal fates (Figures S7I and S8J). The fate choices of Zfp292-OE RPCs approximate but do not fully recapitulate Mettl14-cKO RPCs, which favor late-born bipolar in addition to MG cell fates (Figure S4D). This further supports the theory that *Zfp292* alone is not sufficient to fully recapitulate the Mettl14-cKO phenotypes. Together, our data demonstrate that *Zfp292* is an important target of m^{6}A, although not the only target, and probably works with other m^{6}A-dependent genes to regulate RPC cell-cycle progression and differentiation. Exploring the full effect of manipulating several of the other top candidates, either alone or in combinations, will be an intriguing method to fully expand the m^{6}A pathway in developing RPCs.

In this study we also observed significant upregulation of *Cdkn1a* mRNAs and proteins ($P21^{Cip1}$) in the retina upon m^6A depletion, despite not being a direct m^6A target. This increased expression of $P21^{Cip1}$ is also not directly downstream of *Zfp292*, as overexpression of *Zfp292* did not lead to upregulation of *Cdkn1a* (data not shown). It is interesting to see indirect regulation of $P21^{Cip1}$, a protein involved in cell-cycle-related pathways,[47] by m^6A, and this may be a target for future studies.

Limitations of the study

We were not able to directly confirm whether Mettl14-mediated m^6A modification functions through the mRNA decay pathway in the retina. We attempted to measure the mRNA half-life following published protocols; however, we noticed that most retinal cells died quickly when the retina was placed inside the actinomycin solution (inhibiting transcription). Owing to lack of reagents (e.g., chromatin immunoprecipitation level antibody against Zfp292), we currently cannot identify the direct targets of Zfp292. Because of challenges in long-term live imaging of the retina *ex vivo* (>30 h), we used the FUCCI cell-cycle indicator to estimate the RPC cell-cycle length at early postnatal stages. This experiment suggests that the RPC cell cycle is prolonged but does not directly measure the cell-cycle length. Finally, retrovirus-based lineage tracing may provide more granular details of the differentiation of RPCs at specific stages than EdU pulse-chase analyses. While we have data for RPCs at P1 using retroviruses, a more comprehensive dataset of fate decisions at different time points or with manipulation of different gene targets would provide greater insight into the function of m^6A in regulating the RPC cell cycle.

STAR★METHODS

Detailed methods are provided in the online version of this paper and include the following:

RESOURCE AVAILABILITY

Lead contact—Further information and requests for reagents may be directed to and will be fulfilled by the corresponding author Sui Wang (suiwang@stanford.edu).

Materials availability—Further information and requests for reagents will be fulfilled by the corresponding author Sui Wang (suiwang@stanford.edu). A list of critical reagents is included in the key resources table.

Data and code availability

- Single-cell RNA-seq, m^6A-seq and RNA-seq data have been deposited (GEO: GSE206013, GSE206014 and GSE229872) and are publicly available as of the date of publication. Original western blot and dot blot images have been deposited (Mendeley data: https://doi.org/10.17632/cs8xwknckf.1) and are publicly available as of the date of publication. Microscopy data reported in this paper will be shared by the lead contact upon request.
- This paper does not report the original code.

- Any additional information required to reanalyze the data reported in this work paper is available from the lead contact upon request.

EXPERIMENTAL MODEL AND STUDY PARTICIPANT DETAILS

The *Mettl14*$^{f/f}$ mouse line was a gift from Dr. Chuan He at the University of Chicago.[13] The Chx10-EGFP/Cre mice were purchased from the Jackson Lab (Stock# 005105). Wild-type mouse neonates were obtained from timed pregnant CD1 mice (Charles River Laboratories, #022). All mice were housed on a 12/12-h light/dark cycle at 25°C with unlimited food and water. Both male and female mice were used in the study, with developmental stages including embryonic E13.5, E15.5, postnatal P0, P3–10, P14, P21 and P56. No gender differences were found in all experiments. All animal studies were approved by the Administrative Panel on Laboratory Animal Care (APLAC) at Stanford University.

METHOD DETAILS

Plasmid construction—The *CAG-GFP, CAG-LoxP-Stop-LoxP-GFP, CAG-Cre*, and *CAG-LacZ-shRNA* and *CAG-filler* plasmids were from Wang et al. 2014.[22] To generate the *CAG-Zfp292-op* plasmid, we codon optimized the mouse *Zfp292* ORF and split it into four overlapping DNA fragments (each about ~2kb, Table S1), which were then synthesized by IDT. We cloned these fragments into the *CAG-GFP* backbone by Gibson Assembly to replace *GFP* (NEB, Cat. No. E2611). The *CAG-FUCCI* plasmid was generated by replacing *GFP* of the *CAG-GFP* plasmid with the FUCCI fragment from Addgene plasmid 92139 (Addgene #92139). The *CAG-Zfp292-shRNA* plasmid was generated by inserting the *Zfp292-shRNA* cassette into the 3′UTR of the *mCherry* gene following published protocol.[22] Primers and sequences are listed in Table S1.

Western blot—Mouse retinas were freshly dissected out, transferred to RIPA buffer (Radioimmunoprecipitation assay buffer, Abcam #ab156034), and heated at 95°C for 10 min. Protein concentrations were measured by BCA protein kit (Pierce BCA Protein Assay Kit #23228). Equal amounts of proteins were loaded onto a 4%–20% SDS-PAGE gel (Bio-rad, #4561094) and run at 130V and 30A for 1.5 h. The gel was transferred to a 0.2mm PVDF membrane (BIO-RAD, #1704156) using a semi-dry transfer system (BIO-RAD, 1704150EDU). The membrane was blocked with 5% non-fat milk blocking solution and incubated with primary antibodies at 4°C overnight. Primary antibodies included rabbit anti-Mettl14 (Sigma-Aldrich, HPA038002 1:1000) and rabbit anti-GAPDH (Abcam, ab9485, 1:1000). The membrane was washed with 1X TBST (20mM Tris, 150mM NaCl, 0.1% Tween 20) for 30 min and incubated with secondary antibody conjugated to horseradish peroxidase (Amersham, NA934-100U, 1:5000) at room temperature for 2 h. The membrane was washed again and incubated with the SuperSignal West Pico PLUS chemiluminescent substrate mix (Thermo Scientific, #34580). Chemiluminescent signals were detected using the Amersham ImageQuant 600 (Cytiva) imaging system.

Quantitative real-time PCR—Total RNA was isolated from retinal tissues using QIAGEN RNeasy kit (QIAGEN, 74104). The cDNA was generated using SuperScript III First-Strand Synthesis Kit (Invitrogen, 18080051). qPCR primers were listed in Table S1. The SYBR Green Master Mix (Fisher Scientific, A25742) was used for qPCR. The

qPCR experiments were performed using a Quantstudio3 Real-Time PCR System (Applied Biosystems, A28567) with the following conditions: 50°C for 2 min, 95°C for 10 min, followed by 40 cycles of 95°C for 15s, 60°C for 1min.

Ex vivo* and *in vivo* plasmid electroporation into the retina—Ex vivo* and *in vivo* retina electroporation was carried out as previously described[6,18,22,51] using the FemtoJet 4i microinjector (Eppendorf, Cat#5252000021) and NEPA21 Electroporator (Bulldog Bio). For *ex vivo* electroporation, 5 pulses of 25V, 50ms each with 950ms intervals were applied to dissected retinas. For *in vivo* electroporation, 5 pulses of 80V, 50ms each with 950ms intervals were applied to neonatal mouse pups. All *ex vivo* and *in vivo* electroporation experiments were repeated with at least three biological replicates. Plasmids were electroporated with a concentration of 500ng/ul to 1ug/ul per plasmid.

Histology and immunofluorescence—Mouse eyeballs were fixed in 4% paraformaldehyde (PFA) in 1x PBS (pH 7.4) for 2 h at room temperature. Retinas were then dissected out and equilibrated at room temperature in a series of sucrose solutions (5% sucrose in 1x PBS, 5 min; 15% sucrose in 1x PBS, 15 min; 30% sucrose in 1x PBS, 1 h; 1:1 mixed solution of OCT and 30% sucrose in PBS, 4°C, overnight), embedded in OCT and stored at −80°C. A Leica CM3050S cryostat (Leica Microsystems) was used to prepare 20μm cryosections. Retinal cryosections were washed in 1x PBS briefly, incubated in 0.2% Triton, 1x PBS for 20 min, and blocked for 30 min in blocking solution (0.1% Triton, 1% BSA and 10% donkey serum in 1x PBS, Jackson Immuno Research Laboratories). Slides were incubated with primary antibodies diluted in blocking solution in a humidified chamber at 4°C overnight. After washing in 0.1% Triton 1x PBS for three times, slides were incubated with secondary antibodies and DAPI (Sigma-Aldrich; D9542) for 1 h, then washed for three times with 0.1% Triton, 1x PBS and mounted in Fluoromount-G (Southern Biotechnology Associates). The following primary antibodies were used: chicken anti-GFP (Abcam, ab13970, 1:1000), rabbit anti-Sox9 (Abcam, ab185966, 1:500), rabbit anti-Pax6 (Thermo Fisher Scientific, 42-6600, 1:500), mouse anti-Rhodopsin (Abcam, ab5417, 1:200), mouse anti-Bassoon (Abcam, ab82958, 1:200), mouse anti-Ki67 (BD Biosciences, 550609, 1:200), rabbit anti-P21 (1:500, Abcam, ab188224), Sheep anti-Chx10 (Exalpha Biologicals, X1179P, 1:100), Gunine Pig anti-RBPMS (PhosphoSolutions, 1832-RBPMS, 1:500), mouse anti-Calbindin (Sigma-Aldrich, C9848, 1:500), mouse anti-Rhodopsin (Abcam, ab5417, 1:200), Rabbit anti-GFAP (Fisher Scientific, NC9604017, 1:200), rabbit anti-Mettl14 (Sigma-Aldrich, HPA038002, 1:500) and PNA (Fisher Scientific, NC9604017, 1:200).

TUNEL assay—TUNEL Assay was performed using the Click-iT Plus TUNEL Assay for In Situ Apoptosis Detection, Alexa Fluor 647 dye kit (Invitrogen C10619). Briefly, pre-fixed retinal slides were incubated with TdT reaction buffer for 10 min and then incubated with TdT reaction mixture for 60 min at 37°C. Slides were washed with 3% BSA in PBS for 5 min then incubated with Click-it Plus TUNEL reaction cocktail for 30 min at 37°C.

EdU pulse-chase assay—One microliter of EdU (5μM) was injected intravitreally into mice pups at P3 and P7 using the femtoJet microinjection system. EdU signals were detected on retinal cryosections using the EdU Cell Proliferation Kit (Invitrogen, C10340). Briefly,

retinal slides were washed with 3% BSA in 1xPBS for 5 min and then incubated with Click-it reacting cocktail solutions for 30 min at room temperature, protected from light. After removing the reaction cocktail, slides were washed with 3% BSA in 1x PBS and proceeded to antibody staining.

m^{6}A dot-blot assay—The mRNAs were purified by Dynabeads mRNA DIRECT purification kit (Thermo Fisher Scientific 61011) from 4 control or Mettl14-cKO retinas. mRNA samples were denatured at 95°C, spotted onto Hybond-N+ membrane (Catalog No. GERPN1510B; GE Healthcare) and crosslinked using a Stratalinker 2400 UV crosslinker. Membranes were blocked with 5% milk blocking solution for 1 h, and then incubated with anti-m^{6}A antibody (Synaptic Systems, 202003) for 2 h at room temperature. Membranes were washed and incubated with HRP-conjugated secondary antibodies for 1 h at room temperature. For signal detection, membrane was incubated with ECL Western Blotting Substrate for 5 min in darkness at room temperature and then imaged using the Amersham ImageQuant 600 (Cytiva) imaging system.

mRNA *in situ* hybridization—The probes for mRNA *in situ* hybridization were purchased ACD. The mRNA *in situ* on cryosections or dissociated cells were performed using the RNAscope Multiplex Fluorescent Detection Reagents V2 (ACD, 323110) following commercial protocols.

Retrovirus preparation and delivery in the retina—The *LIA-Cre* and *LIA* plasmids were gifts from Dr. Connie Cepko (Harvard Medical School, Boston, MA, USA). Retrovirus were packaged using HEK293T cells (ATCC-CRL-3216) and purified using ultracentrifuge following published protocols (Turner and Cepko 1987). 0.5μL of LIA-AP/LIA-Cre (3X10^7 CFU/mL) viruses were delivered into the sub-retinal space of P1 mice as previously described (Wang et al. 2014). Retinas were harvested and dissected out at P14, fixed in 4% paraformaldehyde, and stained for alkaline phosphatase activity (AP) using X-phos/NBT kit (FieldsBerry et al., 1992). After embedding in OCT (VWR, 25608-930), retinas were cryo-sectioned at 20 μm thickness and imaged under the Keyence microscope (BZ-800E).

Imaging and analysis—All images of retinal sections and dissociated retinal cells were acquired by a Zeiss LSM880 inverted confocal microscope. Representative images were maximum projections of 5–10mm tissues and were quantified by Fiji software.

m^{6}A-seq (MeRIP-seq) and data analysis—Total RNA was extracted from retina tissues using RNeasy Mini Kit (QIAGEN, 74104). Approximately 30ug of total RNA per sample with RIN >8.0 was used for m^{6}A-seq. The poly(A) mRNAs were isolated by using the Dynabeads Oligo(dT) kit (ThermoFisher, #61002), fragmented into ~100bp-long oligonucleotides using divalent cations under elevated temperature, and incubated with m^{6}A antibody (No. 202003, Synaptic Systems, Germany) in IP buffer (50 mM Tris-HCl, 750 mM NaCl and 0.5% Igepal CA-630) supplemented with BSA (0.5 μg μL–1) for 2 h at 4°C. The mixture was then incubated with protein-A beads and eluted with elution buffer (1 × IP buffer and 6.7mM m6A). Eluted RNAs were precipitated by 75% ethanol. Eluted m6A-containing fragments (IP) and untreated input control fragments are converted to cDNA

libraries and submitted for next generation sequencing (LC-BIO Bio-tech ltd, Hangzhou, China). The sequencing quality was verified by using FastQC. Bowtie was used to map the reads to the Mus musculus (Version: v96) genome with default parameters. Mapped reads of IP and input libraries were provided for R package exomePeak to identify m^6A peaks adapted for visualization on the UCSC genome browser or IGV software. Motifs were identified and localized by using MEME scripts.[52] Called peaks were annotated by intersection with gene architecture using ChIPseeker.[48] StringTie[49] was used to perform expression analyses for all mRNAs from input libraries by calculating FPKM (total exon fragments/mapped reads(millions)×exon length(kB)). The differentially expressed mRNAs were selected with |log2 (fold change) |>1 and p value <0.05 by R package edgeR. GO term analysis was performed by The Gene Ontology Resource (http://geneontology.org/).

Single cell RNA sequencing (scRNA-seq) and data analysis—Retinal tissues were dissociated as described previously[22] and loaded on a 10x Genomics Chromium controller to generate single cell Gel-Beads-in Emulsion (GEMs). Single-cell RNA-Seq libraries were prepared using the Chromium Gene Expression 3′ kit v3.1 (PN-1000269). The quality of the libraries was analyzed by a 2100 Bioanalyzer (Agilent) using a high-sensitivity DNA kit (Agilent, #5067−4626). The libraries were sequenced by Illumina HiSeq4000 platform (2 × 75 pair-end reads). Single cell RNA expression matrices were generated by aligning sequencing reads to a pre-build mouse reference (mm10-2020-A) using the Cell Ranger (v.6.1.1) pipeline and loaded into R (v.4.1) for downstream analyses. We applied SoupX,[53] DoubleDecon[54] and DoubletFinder[55] to remove ambient RNA and doublets. The filtered matrices were processed with Seurat (v.4.1) for quality control, clustering and visualization using standard workflows. Briefly, genes that were detected in fewer than 5 cells, and cells with fewer than 500 genes or more than 5% reads as mitochondrial were excluded from analyses. Control and Mettle14-cKO samples were normalized by SCTransform method[50] and integrated using 3000 variable genes *(PrepSCTIntegration, FindIntegrationAnchors and IntegrateData*). Clusters were generated based on the top 30 principal components (PCs) (*FindNeighbors* function and *FindClusters* function, resolution = 1) and visualized by t-distributed Stochastic Neighbor Embedding (tSNE). To identify the conserved markers of each cluster, we performed differential gene expression tests on each cluster versus all other clusters (*FindConservedMarkers*). Clusters were assigned to 15 major cell types by their conserved markers. Differentially expressed genes (DEGs) were identified using a Wilcoxon rank-sum test (*FindAllMarkers*) between control and Mettl14-cKO in each cell type. DEGs with |log2 (fold change)| > 1 and p value <0.05 were selected as input for GO analysis described above. To query the P7 Mettl14-cKO RPCs on published reference datasets (Clark et al. 2019), the Unimodal UMAP projection function (*Mapquery*, Seurat 4.0.6) was used.

Bulk RNA-seq and data analysis—Approximately 2500 retinal cells were collected via FACS sorting. The cells were directly sorted into lysis buffer provided by the SMART-seq V4 ultra-low input RNA kit for sequencing (Takara Bio 634888). The cDNA libraries were generated following the SMART-seq protocol. The sequencing libraries were prepared by Nextera XT DNA sample preparation Kit (Ilumina, FC-131-1024) and sequenced by Illumina HiSeq4000 platform (2×75 paired-end). The data were processed and analyzed in

Bioconductor with packages including Rfastp, ShortRead, DESeq2, Rsubread, Rsamtools, ClusterProfiler, and ggplot2.

QUANTIFICATION AND STATISTICAL ANALYSIS

All statistics were done as described in figure legends. GraphPad Prism v.9 (GraphPad) was used to perform statistical analyses. Graphs and error bars reflect means ± SD. Unpaired t test with Welch's correction (two-tailed) was used in the study. Statistical significance was defined as a p value < 0.05, where * represents $p < 0.05$, ** represents $p < 0.01$, *** represents $p < 0.001$, **** represents $p < 0.0001$, and "ns" represents $P \geq 0.05$. N number is indicated in figures.

Supplementary Material

Refer to Web version on PubMed Central for supplementary material.

ACKNOWLEDGMENTS

Support was provided by NIH-1R01EY03258501 (to S.W.), 1R01EY03379201 (to S.W.), 5T32EY027816-05 (to S.H.S.), and P30 (P30-EY026877) to Stanford Ophthalmology (to all authors). The content is solely the responsibility of the authors and does not necessarily represent the official views of the National Institutes of Health.

REFERENCES

1. Hardwick LJA, and Philpott A (2014). Nervous decision-making: to divide or differentiate. Trends Genet. 30, 254–261. 10.1016/j.tig.2014.04.001. [PubMed: 24791612]
2. Hardwick LJA, Ali FR, Azzarelli R, and Philpott A (2015). Cell cycle regulation of proliferation versus differentiation in the central nervous system. Cell Tissue Res. 359, 187–200. 10.1007/s00441-014-1895-8. [PubMed: 24859217]
3. Homem CCF, Repic M, and Knoblich JA (2015). Proliferation control in neural stem and progenitor cells. Nat. Rev. Neurosci. 16, 647–659. 10.1038/nrn4021. [PubMed: 26420377]
4. Miles A, and Tropepe V (2016). Coordinating progenitor cell cycle exit and differentiation in the developing vertebrate retina. Neurogenesis (Austin) 3, e1161697. 10.1080/23262133.2016.1161697. [PubMed: 27604453]
5. Belmonte-Mateos C, and Pujades C (2021). From cell states to cell fates: how cell proliferation and neuronal differentiation are coordinated during embryonic development. Front. Neurosci. 15, 781160. 10.3389/fnins.2021.781160. [PubMed: 35046768]
6. Matsuda T, and Cepko CL (2007). Controlled expression of transgenes introduced by in vivo electroporation. Proc. Natl. Acad. Sci. USA 104, 1027–1032. 10.1073/pnas.0610155104. [PubMed: 17209010]
7. Turner DL, and Cepko CL (1987). A common progenitor for neurons and glia persists in rat retina late in development. Nature 328, 131–136. 10.1038/328131a0. [PubMed: 3600789]
8. Alexiades MR, and Cepko C (1996). Quantitative analysis of proliferation and cell cycle length during development of the rat retina. Dev. Dynam. 205, 293–307. 10.1002/(SICI)1097-0177(199603)205:3<293::AID-AJA9>3.0.CO;2-D.
9. Cepko CL, Austin CP, Yang X, Alexiades M, and Ezzeddine D (1996). Cell fate determination in the vertebrate retina. Proc. Natl. Acad. Sci. USA 93, 589–595. [PubMed: 8570600]
10. Yu J, She Y, and Ji S-J (2021). m6A modification in mammalian nervous system development, functions, disorders, and injuries. Front. Cell Dev. Biol. 9, 679662. [PubMed: 34113622]
11. Jiang X, Liu B, Nie Z, Duan L, Xiong Q, Jin Z, Yang C, and Chen Y (2021). The role of m6A modification in the biological functions and diseases. Signal Transduct. Targeted Ther. 6, 74–16. 10.1038/s41392-020-00450-x.

12. Yang Y, Hsu PJ, Chen Y-S, and Yang Y-G (2018). Dynamic transcriptomic m6A decoration: writers, erasers, readers and functions in RNA metabolism. Cell Res. 28, 616–624. 10.1038/s41422-018-0040-8. [PubMed: 29789545]

13. Yoon K-J, Ringeling FR, Vissers C, Jacob F, Pokrass M, Jimenez-Cyrus D, Su Y, Kim N-S, Zhu Y, Zheng L, et al. (2017). Temporal control of mammalian cortical neurogenesis by m6A methylation. Cell 171, 877–889. 10.1016/j.cell.2017.09.003. [PubMed: 28965759]

14. Wang Y, Li Y, Yue M, Wang J, Kumar S, Wechsler-Reya RJ, Zhang Z, Ogawa Y, Kellis M, Duester G, and Zhao JC (2018). N6-methyladenosine RNA modification regulates embryonic neural stem cell self-renewal through histone modifications. Nat. Neurosci. 21, 195–206. 10.1038/s41593-017-0057-1. [PubMed: 29335608]

15. Rowan S, and Cepko CL (2004). Genetic analysis of the homeodomain transcription factor Chx10 in the retina using a novel multifunctional BAC transgenic mouse reporter. Dev. Biol. 271, 388–402. 10.1016/j.ydbio.2004.03.039. [PubMed: 15223342]

16. Dick O, tom Dieck S, Altrock WD, Ammermüller J, Weiler R, Garner CC, Gundelfinger ED, and Brandstätter JH (2003). The presynaptic active zone protein bassoon is essential for photoreceptor ribbon synapse formation in the retina. Neuron 37, 775–786. 10.1016/s0896-6273(03)00086-2. [PubMed: 12628168]

17. Buck SB, Bradford J, Gee KR, Agnew BJ, Clarke ST, and Salic A (2008). Detection of S-phase cell cycle progression using 5-ethynyl-2′-deoxyuridine incorporation with click chemistry, an alternative to using 5-bromo-2′-deoxyuridine antibodies. Biotechniques 44, 927–929. 10.2144/000112812. [PubMed: 18533904]

18. Matsuda T, and Cepko CL (2004). Electroporation and RNA interference in the rodent retina in vivo and in vitro. Proc. Natl. Acad. Sci. USA 101, 16–22. 10.1073/pnas.2235688100. [PubMed: 14603031]

19. Venters SJ, Mikawa T, and Hyer J (2015). Early divergence of centraland peripheral neural retina precursors during vertebrate eye development. Dev. Dynam. 244, 266–276. 10.1002/dvdy.24218.

20. Sakaue-Sawano A, Kurokawa H, Morimura T, Hanyu A, Hama H, Osawa H, Kashiwagi S, Fukami K, Miyata T, H, M., et al. (2008). Visualizing spatiotemporal dynamics of multicellular cell-cycle progression. Cell 132, 487–498. 10.1016/j.cell.2007.12.033. [PubMed: 18267078]

21. Nora EP, Goloborodko A, Valton A-L, Gibcus JH, Uebersohn A, Abdennur N, Dekker J, Mirny LA, and Bruneau BG (2017). Targeted degradation of CTCF decouples local insulation of chromosome domains from genomic compartmentalization. Cell 169, 930–944.e22. 10.1016/j.cell.2017.05.004. [PubMed: 28525758]

22. Wang S, Sengel C, Emerson MM, and Cepko CL (2014). A gene regulatory network controls the binary fate decision of rod and bipolar cells in the vertebrate retina. Dev. Cell 30, 513–527. 10.1016/j.devcel.2014.07.018. [PubMed: 25155555]

23. Delatte B, Wang F, Ngoc LV, Collignon E, Bonvin E, Deplus R, Calonne E, Hassabi B, Putmans P, Awe S, et al. (2016). Transcriptome-wide distribution and function of RNA hydroxymethylcytosine. Science 351, 282–285. 10.1126/science.aac5253. [PubMed: 26816380]

24. Chen T, Hao Y-J, Zhang Y, Li M-M, Wang M, Han W, Wu Y, Lv Y, Hao J, Wang L, et al. (2015). m(6)A RNA methylation is regulated by microRNAs and promotes reprogramming to pluripotency. Cell Stem Cell 16, 289–301. 10.1016/j.stem.2015.01.016. [PubMed: 25683224]

25. Zhang C, Fu J, and Zhou Y (2019). A review in research progress concerning m6A methylation and immunoregulation. Front. Immunol. 10, 922. [PubMed: 31080453]

26. Gudmundsdottir K, and Ashworth A (2006). The roles of BRCA1 and BRCA2 and associated proteins in the maintenance of genomic stability. Oncogene 25, 5864–5874. 10.1038/sj.onc.1209874. [PubMed: 16998501]

27. Cantor SB, and Guillemette S (2011). Hereditary breast cancer and the BRCA1-associated FANCJ/BACH1/BRIP1. Future Oncol. 7, 253–261. 10.2217/fon.10.191. [PubMed: 21345144]

28. Zona S, Bella L, Burton MJ, Nestal de Moraes G, and Lam EW-F (2014). FOXM1: an emerging master regulator of DNA damage response and genotoxic agent resistance. Biochim. Biophys. Acta 1839, 1316–1322. 10.1016/j.bbagrm.2014.09.016. [PubMed: 25287128]

29. Wei J-H, Chou Y-F, Ou Y-H, Yeh Y-H, Tyan S-W, Sun T-P, Shen C-Y, and Shieh S-Y (2005). TTK/hMps1 participates in the regulation of DNA damage checkpoint response by phosphorylating

CHK2 on threonine 68. J. Biol. Chem. 280, 7748–7757. 10.1074/jbc.M410152200. [PubMed: 15618221]

30. Lens SMA, Wolthuis RMF, Klompmaker R, Kauw J, Agami R, Brummelkamp T, Kops G, and Medema RH (2003). Survivin is required for a sustained spindle checkpoint arrest in response to lack of tension. EMBO J. 22, 2934–2947. 10.1093/emboj/cdg307. [PubMed: 12805209]
31. Clark BS, Stein-O'Brien GL, Shiau F, Cannon GH, Davis-Marcisak E, Sherman T, Santiago CP, Hoang TV, Rajaii F, James-Esposito RE, et al. (2019). Single-cell RNA-seq analysis of retinal development identifies NFI factors as regulating mitotic exit and late-born cell specification. Neuron 102, 1111–1126. 10.1016/j.neuron.2019.04.010. [PubMed: 31128945]
32. Zhou L, Fu L, Lv N, Liu J, Li Y, Chen X, Xu Q, Chen G, Pang B, Wang L, et al. (2018). Methylation-associated silencing of BASP1 contributes to leukemogenesis in t(8;21) acute myeloid leukemia. Exp. Mol. Med. 50, 1–8. 10.1038/s12276-018-0067-4.
33. Wang M, Niu W, Hu R, Wang Y, Liu Y, Liu L, Zhong J, Zhang C, You H, Zhang J, et al. (2019). POLR1D promotes colorectal cancer progression and predicts poor prognosis of patients. Mol. Carcinog. 58, 735–748. 10.1002/mc.22966. [PubMed: 30582221]
34. Liang L, Haug JS, Seidel CW, and Gibson MC (2014). Functional genomic analysis of the periodic transcriptome in the developing Drosophila wing. Dev. Cell 29, 112–127. 10.1016/j.devcel.2014.02.018. [PubMed: 24684830]
35. Bhargava S, Patil V, Shah RA, and Somasundaram K (2018). IGF2 mRNA binding protein 3 (IMP3) mediated regulation of transcriptome and translatome in glioma cells. Cancer Biol. Ther. 19, 42–52. 10.1080/15384047.2017.1323601. [PubMed: 28485999]
36. Gong W, Xu J, Wang G, Li D, and Zhan Q (2021). ZNF292 suppresses proliferation of ESCC cells through ZNF292/SKP2/P27 signaling axis. Chin. J. Cancer Res. 33, 637–648. 10.21147/j.issn.1000-9604.2021.06.01. [PubMed: 35125808]
37. Karimian A, Ahmadi Y, and Yousefi B (2016). Multiple functions of p21 in cell cycle, apoptosis and transcriptional regulation after DNA damage. DNA Repair 42, 63–71. 10.1016/j.dnarep.2016.04.008. [PubMed: 27156098]
38. Kumari R, and Jat P (2021). Mechanisms of cellular senescence: cell cycle arrest and senescence associated secretory phenotype. Front. Cell Dev. Biol. 9, 645593. 10.3389/fcell.2021.645593. [PubMed: 33855023]
39. Takeda H, Wei Z, Koso H, Rust AG, Yew CCK, Mann MB, Ward JM, Adams DJ, Copeland NG, and Jenkins NA (2015). Transposon mutagenesis identifies genes and evolutionary forces driving gastrointestinal tract tumor progression. Nat. Genet. 47, 142–150. 10.1038/ng.3175. [PubMed: 25559195]
40. Lee JH, Song SY, Kim MS, Yoo NJ, and Lee SH (2016). Frameshift mutations of a tumor suppressor gene ZNF292 in gastric and colorectal cancers with high microsatellite instability. APMIS : APMIS 124, 556–560. 10.1111/apm.12545. [PubMed: 27150435]
41. Wang F, Flanagan J, Su N, Wang L-C, Bui S, Nielson A, Wu X, Vo H-T, Ma X-J, and Luo Y (2012). RNAscope. J. Mol. Diagn. 14, 22–29. 10.1016/j.jmoldx.2011.08.002. [PubMed: 22166544]
42. De Biase D, Prisco F, Piegari G, Ilsami A, d'Aquino I, Baldassarre V, Zito Marino F, Franco R, Papparella S, and Paciello O (2021).RNAScope in situ hybridization as a novel technique for the assessment of c-KIT mRNA expression in canine mast cell tumor. Front. Vet. Sci. 8, 591961. [PubMed: 33665215]
43. Edens BM, Vissers C, Su J, Arumugam S, Xu Z, Shi H, Miller N, Rojas Ringeling F, Ming G-L, He C, et al. (2019). FMRP modulates neural differentiation through m6A-dependent mRNA nuclear export. Cell Rep. 28, 845–854. 10.1016/j.celrep.2019.06.072. [PubMed: 31340148]
44. Li M, Zhao X, Wang W, Shi H, Pan Q, Lu Z, Perez SP, Suganthan R, He C, Bjørås M, and Klungland A (2018). Ythdf2-mediated m6A mRNA clearance modulates neural development in mice. Genome Biol. 19, 69. 10.1186/s13059-018-1436-y. [PubMed: 29855337]
45. Wang C-X, Cui G-S, Liu X, Xu K, Wang M, Zhang X-X, Jiang L-Y, Li A, Yang Y, Lai W-Y, et al. (2018). METTL3-mediated m6A modification is required for cerebellar development. PLoS Biol. 16, e2004880. 10.1371/journal.pbio.2004880. [PubMed: 29879109]

46. Niu F, Han P, Zhang J, She Y, Yang L, Yu J, Zhuang M, Tang K, Shi Y, Yang B, et al. (2022). The m6A reader YTHDF2 is a negative regulator for dendrite development and maintenance of retinal ganglion cells. Elife 11, e75827. 10.7554/eLife.75827. [PubMed: 35179492]

47. Abbas T, and Dutta A (2009). p21 in cancer: intricate networks and multiple activities. Nat. Rev. Cancer 9, 400–414. 10.1038/nrc2657. [PubMed: 19440234]

48. Yu G, Wang L-G, and He Q-Y (2015). ChIPseeker: an R/Bioconductor package for ChIP peak annotation, comparison and visualization. Bioinformatics 31, 2382–2383. 10.1093/bioinformatics/btv145. [PubMed: 25765347]

49. Pertea M, Pertea GM, Antonescu CM, Chang T-C, Mendell JT, and Salzberg SL (2015). StringTie enables improved reconstruction of a transcriptome from RNA-seq reads. Nat. Biotechnol. 33, 290–295. 10.1038/nbt.3122. [PubMed: 25690850]

50. Hafemeister C, and Satija R (2019). Normalization and variance stabilization of single-cell RNA-seq data using regularized negative binomial regression. Genome Biol. 20, 296. 10.1186/s13059-019-1874-1. [PubMed: 31870423]

51. Emerson MM, and Cepko CL (2011). Identification of a retina-specificOtx2 enhancer element active in immature developing photoreceptors. Dev. Biol. 360, 241–255. 10.1016/j.ydbio.2011.09.012. [PubMed: 21963459]

52. Bailey TL, Boden M, Buske FA, Frith M, Grant CE, Clementi L,Ren J, Li WW, and Noble WS (2009). Meme SUITE: tools for motif discovery and searching. Nucleic Acids Res. 37, W202–W208. 10.1093/nar/gkp335. [PubMed: 19458158]

53. Young MD, and Behjati S (2020). SoupX removes ambient RNA contamination from droplet-based single-cell RNA sequencing data. GigaScience 9, giaa151. 10.1093/gigascience/giaa151. [PubMed: 33367645]

54. DePasquale EAK, Schnell DJ, Van Camp P-J, Valiente-Alandí, Í., Blaxall, B.C., Grimes, H.L., Singh, H., and Salomonis, N. (2019). DoubletDecon: deconvoluting doublets from single-cell RNA-sequencing data. Cell Rep. 29, 1718–1727. 10.1016/j.celrep.2019.09.082. [PubMed: 31693907]

55. McGinnis CS, Murrow LM, and Gartner ZJ (2019). DoubletFinder: doublet detection in single-cell RNA sequencing data using artificial nearest neighbors. Cell Syst. 8, 329–337. 10.1016/j.cels.2019.03.003. [PubMed: 30954475]

Highlights

- Depletion of Mettl14 induces retinal developmental delay and neuronal cell death
- Mettl14-depleted late-born RPCs have extended cell-cycle length
- Mettl14-mediated m^6A regulates cell-cycle-related genes in the developing retina
- *Zfp292* is a target of m^6A that inhibits RPC cell-cycle progression

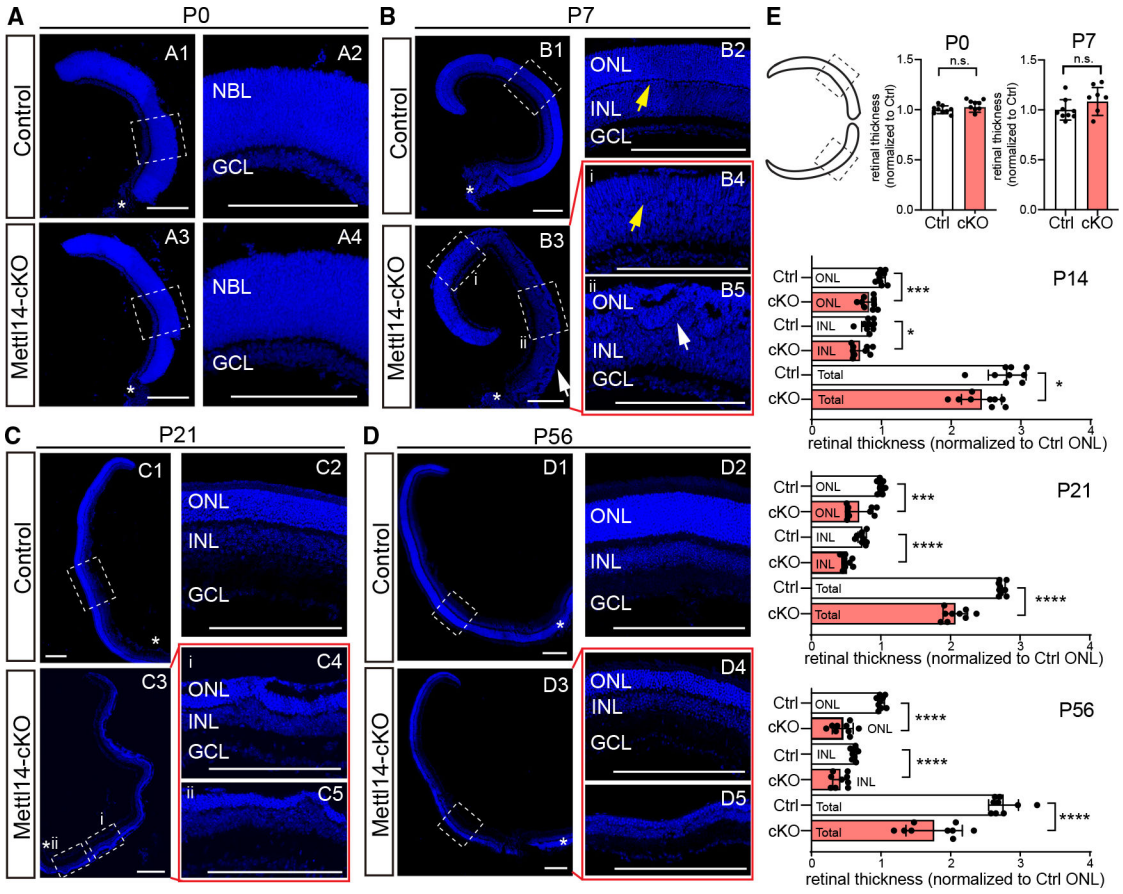

Figure 1. Depletion of Mettl14 results in postnatal retinal developmental defects

(A–D) Retinal morphology at P0 (A), P7 (B), P21 (C), and P56 (D). White stars indicate central retina. In (B), yellow arrows point to OPL and white arrows point to rosette-like structures. A2, A4, B2, B4, B5, C2, C4, C5, D2, D4, and D5 are magnified views of the highlighted regions in A1, A3, B1, B3i, B3ii, C1, C3i, C3ii, D1, D3, and Figure S1L, respectively. NBL, neuroblast layer; ONL, outer nuclear layer; INL, inner nuclear layer; IPL, inner plexiform layer; GCL, ganglion cell layer. Scale bars, 200 μm.

(E) Retinal thickness at P0, P7, P14, P21, and P56. The highlighted regions were quantified. Mean ± SD (n = 6–9 mice; *p < 0.05, ***p < 0.001, ****p < 0.0001, unpaired t test with Welch's correction, two-tailed). ONL, ONL thickness; INL, INL thickness; Total, overall retina thickness; Ctrl, control retina; cKO, Mettl14-cKO retina.

See also Figure S1.

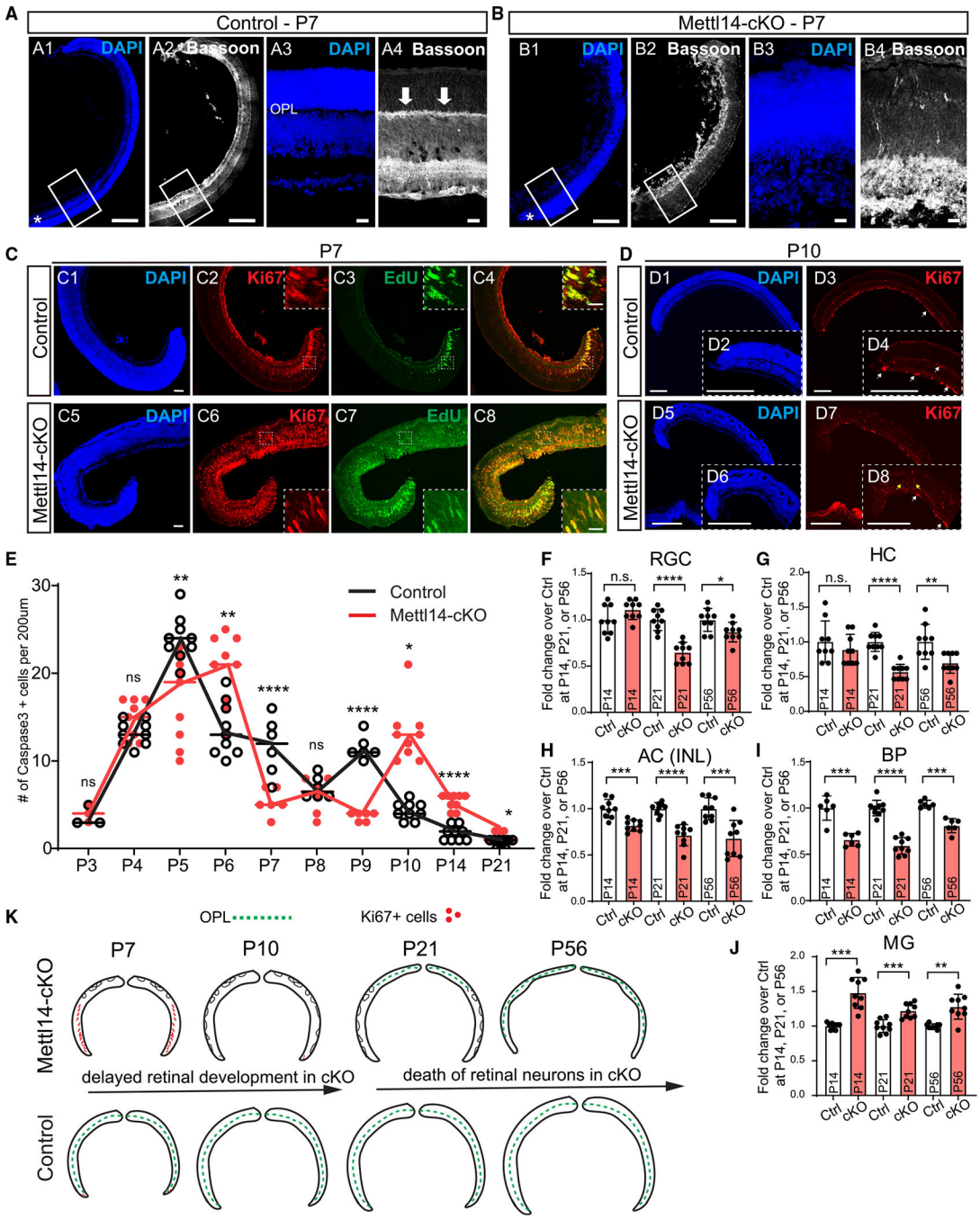

Figure 2. The Mettl14-cKO retina contains excessive RPCs and shows significant neuronal cell death

(A and B) Bassoon staining at P7. White arrows point to OPL. A3/A4 and B3/B4: magnified views of the highlighted regions. Scale bars, 200 μm (A1/A2 and B1/B2) and 20 μm (A3/A4 and B3/B4).

(C) Ki67^{+} and EdU^{+} nuclei in P7 retinas at 2 h post EdU injection. Dashed-line boxes: magnified views of the highlighted regions. Scale bars, 50 μm (C1–C8) and 20 μm (insets).

(D) Ki67 staining at P10. White arrows point to non-specific staining of vessels. Yellow arrows point to Ki67^{+} cells. Scale bars, 200 μm.

(E) Number of Caspase3$^+$ cells from P3 to P21.
(F–J) Number of indicated retinal cell types at P14, P21, and P56. RGC, retinal ganglion cells; HC, horizontal cells; AC (INL), amacrine cells in INL; BP, bipolar cells; MG, Müller glial cells; Ctrl, control retinas; cKO, Mettl14-cKO retinas.
(K) Summary of the observed phenotypes in Mettl14-cKO.
Mean ± SD (E–J, n = 3–9 mice; *p < 0.05, **p < 0.01, ***p < 0.001, ****p < 0.0001, unpaired t test with Welch's correction, two-tailed).
See also Figures S2 and S3.

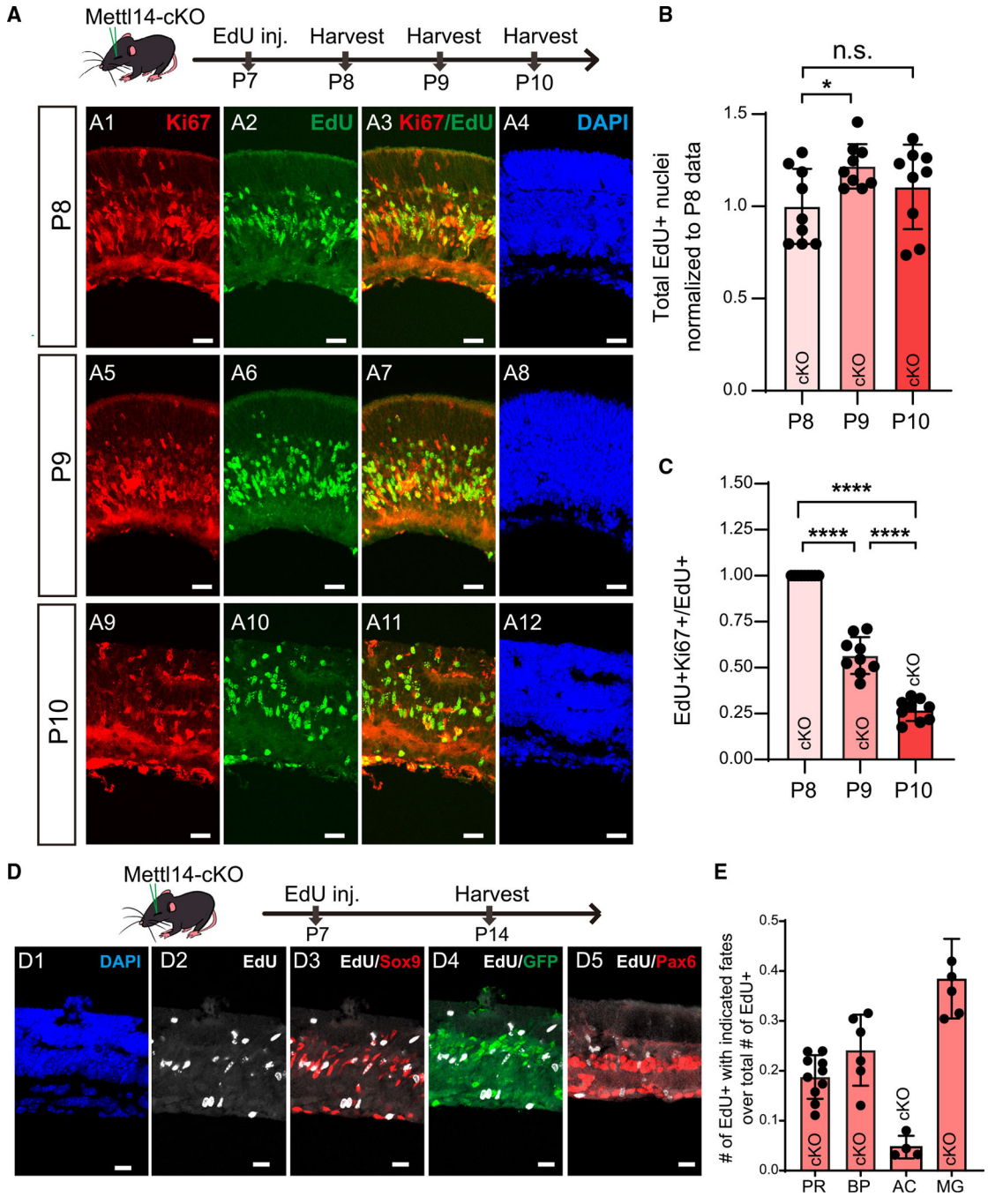

Figure 3. Mettl14-cKO RPCs have extended cell-cycle length

(A) EdU pulse-chase experiment. Scale bars, 20 μm.

(B and C) (B) Number of EdU^+ nuclei at P8, P9, and P10 in Mettl14-cKO after P7 EdU injection. (C) Percentage of cells remaining in the cell cycle ($Ki67^+EdU^+/EdU^+$) at P8, P9, and P10 in Mettl14-cKO after P7 EdU injection. Data normalized to P8 values. Mean ± SD (n = 9 mice; *p < 0.05, ****p < 0.0001, unpaired t test with Welch's correction, two-tailed).

(D) Fates of EdU-labeled P7 Mettl14-cKO RPCs. GFP signals from *Chx10-EGFP/Cre* transgene. $Sox9^+$, Müller glial cells; $Pax6^+Sox9^-$, amacrine cells; GFP^+Sox9^-, bipolar cells. Scale bars, 20 μm.

(E) Percentage of EdU^+ cells adopting indicated fates at P14. Mean ± SD (n ≥ 4 mice).

See also Figures S3 and S4.

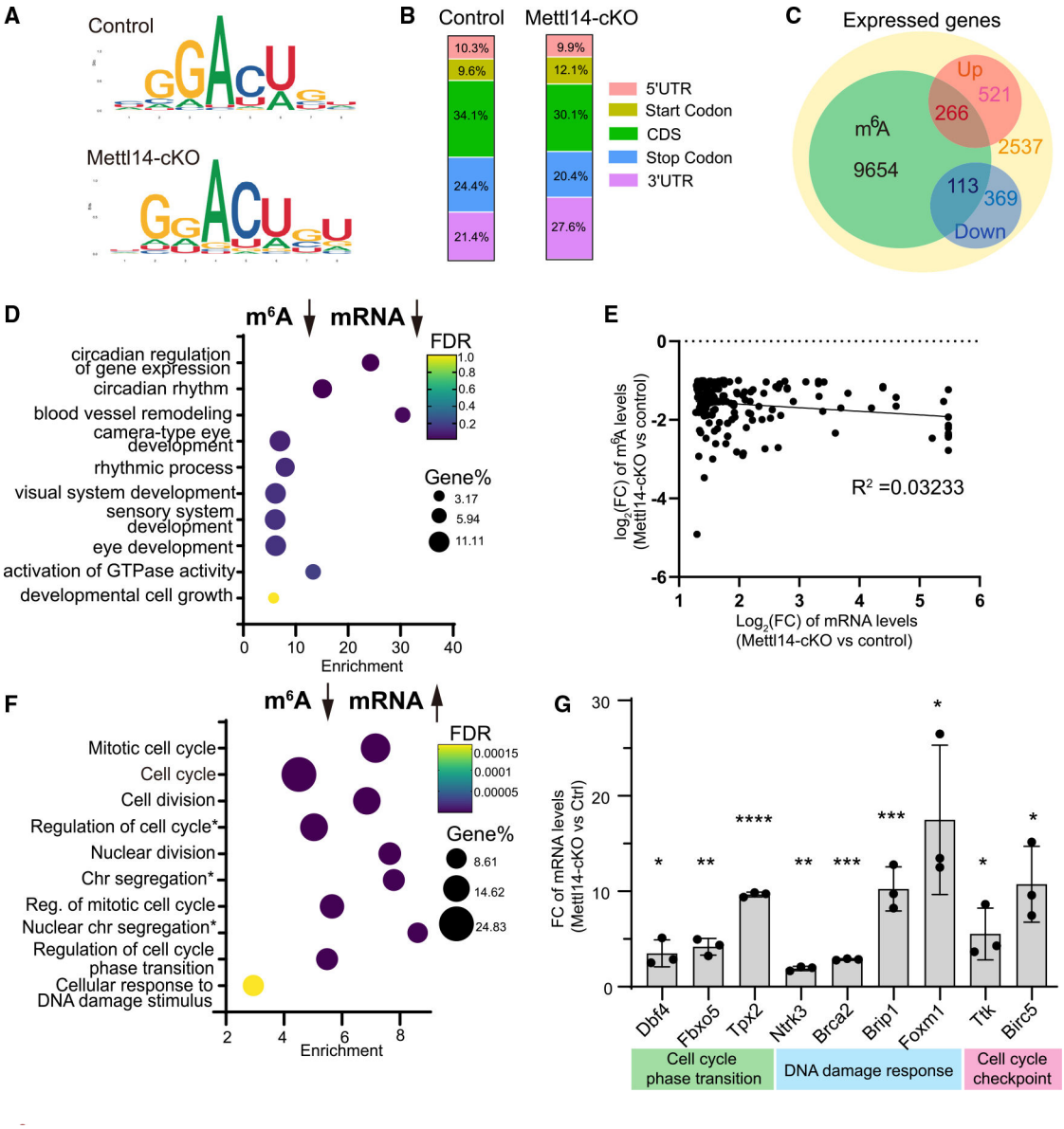

Figure 4. m^{6}A regulates cell-cycle-related genes in the developing retina

(A) Consensus m^{6}A motifs in P7 retinas.

(B) Localization of m^{6}A peaks.

(C) Yellow: genes expressed in control retinas at P7. Green: genes with m^{6}A peaks in control retinas. Red: upregulated genes in Mettl14-cKO. Blue: downregulated genes in Mettl14-cKO.

(D) GO analysis of genes with decreased mRNA and m^{6}A levels in Mettl14-cKO at P7.

(E) Correlation between m^{6}A level decrease and mRNA level increase in P7 Mettl14-cKO retinas ($p < 0.05$).

(F) GO analysis of genes with increased mRNA and decreased m^{6}A levels in Mettl14-cKO at P7. Asterisks denote GO:0010564.

(G) qPCR verification of top candidate genes with increased mRNA and decreased m^{6}A levels in Mettl14-cKO at P7. Known roles of candidate genes are indicated. Values are

normalized to controls. Mean ± SD (n = 3 mice; *p < 0.05, **p < 0.01, ***p < 0.001, ****p < 0.0001, unpaired t test with Welch's correction, two-tailed).
See also Figure S5.

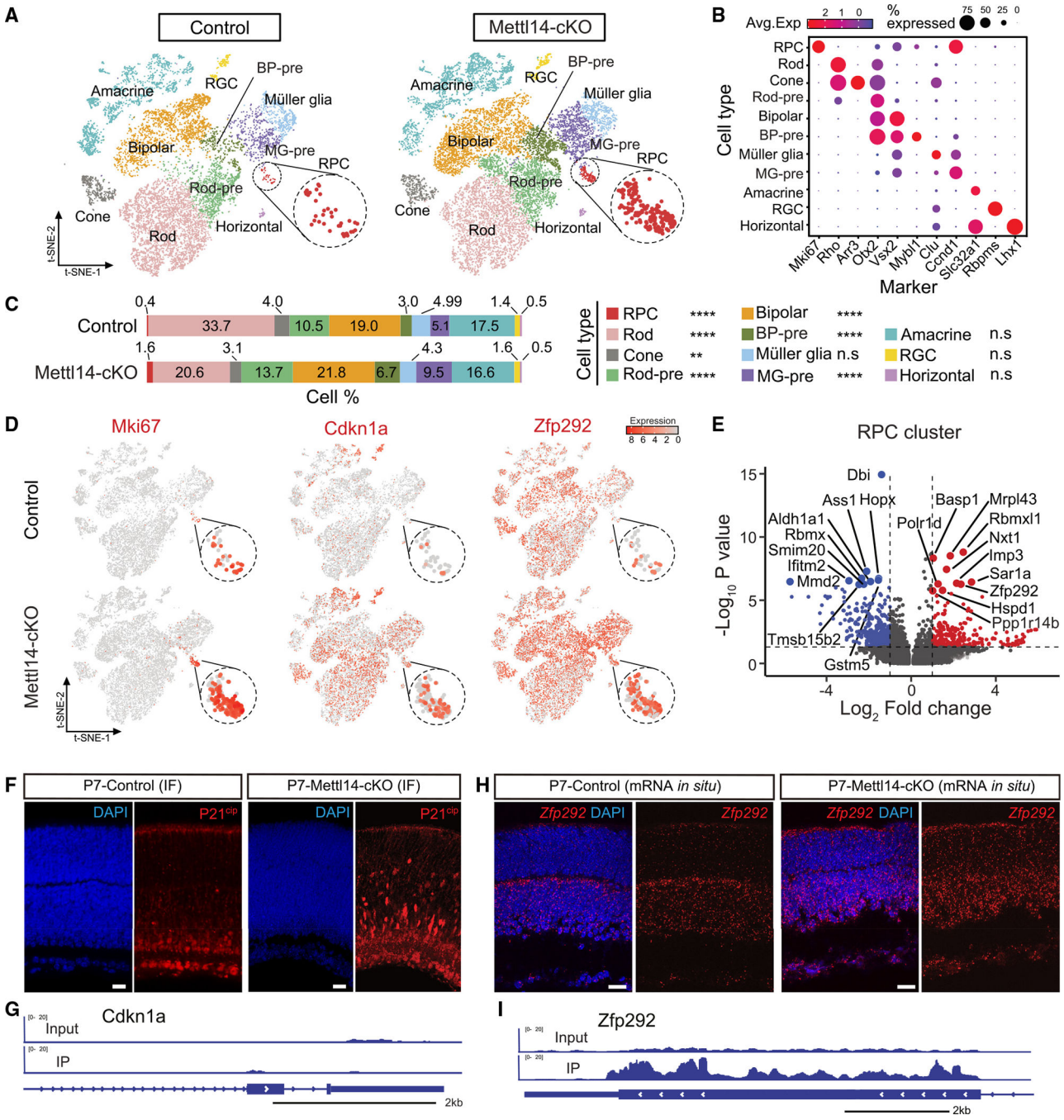

Figure 5. scRNA-seq reveals molecular events downstream of m^{6}A in the developing retina

(A) T-SNE maps of retinal cells at P7 with highlighted RPC clusters as insets.

(B) Markers used for identifying retinal cell types. Dot size: proportion of cells expressing marker genes. Dot color: average expression levels. Rod-pre, rod precursor; BP-pre, bipolar precursor; MG-pre, Müller glia precursor.

(C) Proportion of each cell type at P7 (****p < 0.0001, **p < 0.001, Fisher's exact test followed by Bonferroni correction for multiple comparisons; n.s, not significant).

(D) Expression of *Mki67, Cdkn1a,* and *Zfp292* at P7, with highlighted RPC clusters as insets.

(E) Red: upregulated DEGs in Mettl14-cKO at P7. Blue: downregulated DEGs in Mettl14-cKO at P7. Dashed lines: $p < 0.05$ (Wilcoxon rank-sum test) and $|\log_2 \text{fold change}| > 1$. Top ten DEGs are labeled.

(F) $P21^{cip}$ expression in P7. Scale bars, 20 μm.

(G) m^6A peaks on *Cdkn1a* gene in control P7 retinas.

(H) *Zfp292* mRNA *in situ* in P7 retinas. Scale bars, 20 μm.

(I) m^6A peaks on *Zfp292* gene in control P7 retinas.

See also Figures S5 and S6.

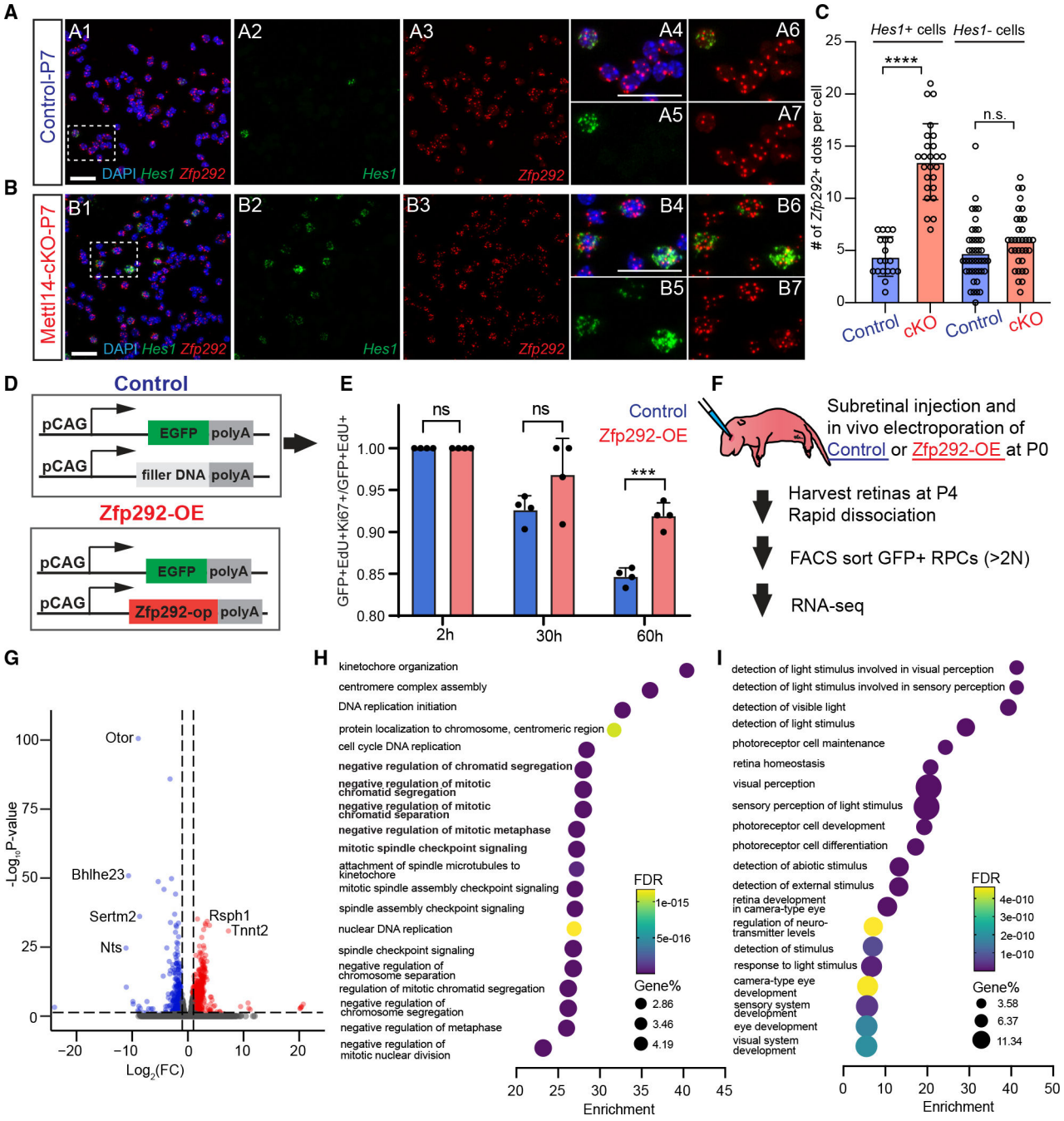

Figure 6. Zfp292 inhibits the cell-cycle progression of postnatal RPCs

(A and B) *Zfp292* and *Hes1* mRNAs levels in dissociated P7 retinal cells. A4–A7 and B4–B7: magnified views of the highlighted regions. Scale bars, 20 μm.

(C) Number of *Zfp292*$^{+}$ mRNA dots per cell in *Hes1*$^{+}$ or *Hes1*$^{-}$ cells. Mean ± SD (n = 3 mice, each data point represents a cell; ****p < 0.0001, unpaired t test with Welch's correction, two-tailed).

(D) Control and *Zfp292*-expressing (Zfp292-OE) plasmids. *Zfp292-op*: codon-optimized mouse *Zfp292*. Filler: plasmid DNA to ensure equivalent plasmid concentration.

(E) Two-hour, 30-h, and 60-h EdU pulse-chase of P0 RPCs expressing *Zfp292* in retinal explants. Control or Zfp292-OE: retinal explants electroporated with "Control" or "Zfp292-OE" plasmids (D). Percentage of GFP^+EdU^+ cells that remain $Ki67^+$ is shown. Mean ± SD (n = 4 mice; ***p < 0.001, unpaired t test with Welch's correction, two-tailed).

(F) Identifying Zfp292 target genes.

(G) DEGs between "Zfp292-OE" and "Control." Dashed lines: p < 0.05 (Wilcoxon rank-sum test) and $|\log_2$ fold change| > 1. Top up or downregulated DEGs are highlighted in red or blue.

(H and I) GO analyses of upregulated (H) or downregulated (I) DEGs in Zfp292-OE RPCs compared with controls.

See also Figures S7 and S8.

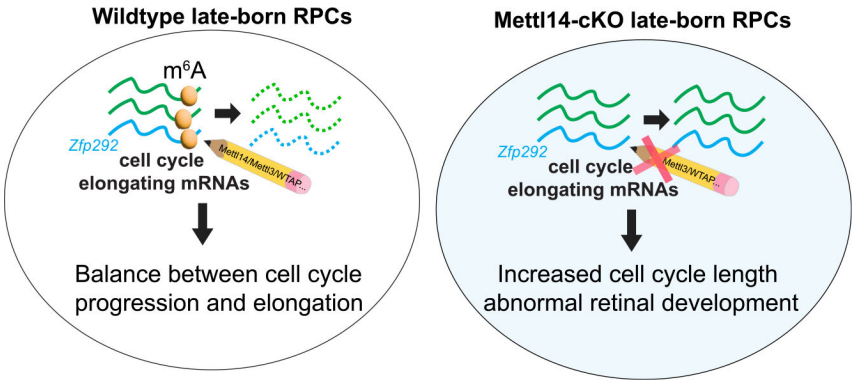

Figure 7. A working model of m^{6}A-mediated cell-cycle regulation in RPCs

KEY RESOURCES TABLE

REAGENT or RESOURCE	SOURCE	IDENTIFIER
Antibodies		
Rabbit polyclonal anti Mettl14	Sigma-Aldrich	Cat#HPA038002; RRID:AB_10672401
Rabbit polyclonal anti GAPDH	Abcam	Cat# ab9485; RRID:AB_307275
Donkey anti rabbit HRP-linked	Cytiva	Cat# NA934-100U; RRID:AB_772206
Chicken polyclonal anti GFP	Abcam	Cat# ab13970; RRID:AB_300798
Rabbit monoclonal anti Sox9	Abcam	Cat# ab185966; RRID:AB_2728660
Rabbit polyclonal anti Pax6	Thermo Fisher Scientific	Cat# 42-6600; RRID:AB_2533534
Mouse monoclonal anti Bassoon	Abcam	Cat# ab82958; RRID:AB_1860018
Mouse monoclonal anti Rhodopsin	Abcam	Cat# ab5417; RRID:AB_304874
Mouse monoclonal anti Ki67	BD Biosciences	Cat# 550609; RRID:AB_393778
Rabbit monoclonal anti p21	Abcam	Cat# ab188224; RRID:AB_2734729
Sheep polyclonal anti chx10	Exalpha	Cat# X1179P; RRID:AB_2889828
Guinea pig polyclonal anti RBPMS	PhosphoSolutions,	Cat# 1832-RBPMS; RRID:AB_2492226
Mouse monoclonal anti Calbindin	Sigma-Aldrich	Cat# C9848; RRID:AB_476894
Chicken polyclonal anti GFAP	Novus Biologicals	Cat# NBP105198; RRID:AB_1556315
Peanut agglutinin (PNA)	Fisher Scientific	Cat# NC9604017; RRID:AB_2336642
Rabbit polyclonal anti m^6A	Synaptic Systems	Cat# 202003; RRID:AB_2279214
Bacterial and virus strains		
LIA-Cre	Made in the lab	Wang et al. 2014[22]
LIA-AP	Made in the lab	Wang et al. 2014[22]
Chemicals, peptides, and recombinant proteins		
SYBR™ Green Master Mix	Fisher Scientific	A25742
PEI (polyethylenimine)	Polysciences Inc	24765-1
stabilized substrate for AP staining	Promega	S3841
Critical commercial assays		
QIAGEN RNeasy Micro Kit for RNA isolation	QIAGEN	74004
SuperScript™ III First-Strand Synthesis Kit	Invitrogen	18080051
Click-iT™ Plus TUNEL Assay	Invitrogen	C10619
Click-iT EdU Assays	Invitrogen	C10640
Dynabeads™ mRNA DIRECT™ Purification Kit	Thermo Scientific	61011
RNAscope™ Multiplex Fluorescent Assay	ACD	320851
scRNA-seq Chromium Gene Expression 3' kit v3.1	10x Genomics	PN-1000269
Deposited data		
Raw sequencing data	This paper	GEO: GSE206013, GSE206014 and GEO229872

REAGENT or RESOURCE	SOURCE	IDENTIFIER
Experimental models: Organisms/strains		
Mouse: Chx10-cre: Chx10-EGFP/cre,-ALPP)2Clc/J	The Jackson Laboratory	JAX: 005105
Mouse: CD1	Charles River Laboratories	Strain Code 022
Mouse: Mettl14$^{f/f}$	(Yoon et al.2017)	N/A
Oligonucleotides		
Primers for qPCR (Table S1)	This paper	N/A
Zfp292-shRNA sequences (Table S1)	This paper	N/A
Gblock gene fragments for making CAG-Zfp292-op (Table S1)	This paper	N/A
Recombinant DNA		
Plasmid: CAG-GFP	Wang et al. 2014[22]	N/A
Plasmid: CAG-LoxP-Stop-LoxP-GFP	Wang et al. 2014[22]	N/A
Plasmid: CAG-Cre	Wang et al. 2014[22]	N/A
Plasmid: CAG-filler	Wang et al. 2014[22]	N/A
Plasmid: CAG-Zfp292-op	This paper	N/A
Plasmid: CAG-FUCCI	This paper	N/A
Plasmid: CAG-mCherry-lacZ-shRNA	Wang et al. 2014[22]	N/A
Plasmid: CAG-mCherry-Zfp292-shRNA	This paper	N/A
Software and algorithms		
Fiji		https://imagej.net/software/fiji/
ChIPseeker	Yu et al. 2015[48]	https://github.com/YuLab-SMU/ChIPseeker
StringTie	Pertea et al. 2015[49]	https://github.com/gpertea/stringtie
SCTransform	Hafemeister and Satija 2019[50]	https://satijalab.org/seurat/articles/sctransform_vignette.html
Prism v.9	GraphPad	https://www.graphpad.com/updates/prism-900-release-notes
Other		
Quantstudio3 Real-Time PCR System	Applied Biosystems	A28567
FemtoJet 4i microinjector	Eppendorf	5252000021
NEPA21 Super Electroporator	NEPA GENE	https://www.nepagene.jp/e_products_nepagene_0001.html
UV crosslinker	Stratagene	https://www.thelabworldgroup.com/product/stratagene-stratalinker-ultraviolet-crosslinker/
10x Genomics Chromium controller	10x Genomics	https://www.10xgenomics.com/instruments/chromium-controller
Semi-dry transfer system	BIO-RAD	1704150EDU
Keyence microscope	Keyence	BZ-800E
Aria Fusion Sorter (FACS)	BD Aria Fusion	https://facs.stanford.edu/instruments/costello
Amersham ImageQuant 600	Cytiva	BZ-800E

REAGENT or RESOURCE	SOURCE	IDENTIFIER
Confocal microscope	Zeiss	LSM880